*J. Fluid Mech.* (2022), *vol*. 943, A41, doi:10.1017/jfm.2022.464

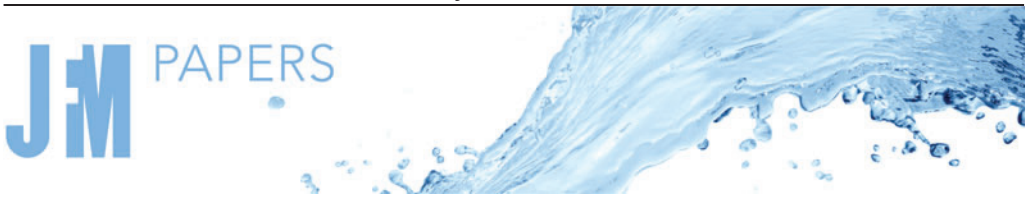


# Topological transition and helicity conversion of vortex knots and links

**Weiyu Shen[1], Jie Yao[2], Fazle Hussain[2] and Yue Yang[1,3,†]**

[1]State Key Laboratory for Turbulence and Complex Systems, College of Engineering, Peking University, Beijing 100871, PR China

[2]Department of Mechanical Engineering, Texas Tech University, Lubbock, TX 79409, USA

[3]HEDPS-CAPT and BIC-ESAT, Peking University, Beijing 100871, PR China

(Received 20 September 2021; revised 20 May 2022; accepted 23 May 2022)

Topological transition and helicity conversion of vortex torus knots and links are studied using direct numerical simulations of the incompressible Navier–Stokes equations. We find three topological transitional routes (*viz.* merging, reconnection and transition to turbulence) in the evolution of vortex knots and links over a range of torus aspect ratios and winding numbers. The topological transition depends not only on the initial topology but also on the initial geometry of knots/links. For small torus aspect ratios, the initially knotted or linked vortex tube rapidly merges into a vortex ring with a complete helicity conversion from the writhe and link components to the twist. For large torus aspect ratios, the vortex knot or link is untied into upper and lower coiled loops via the first vortex reconnection, with a helicity fluctuation including loss of writhe and link, and generation of twist. Then, the relatively unstable lower loop can undergo a secondary reconnection to split into multiple small vortices with a similar helicity fluctuation. Surprisingly, for moderate torus aspect ratios, the incomplete reconnection of tangled vortex loops together with strong vortex interactions triggers transition to turbulence, in which the topological helicity decomposition fails due to the breakdown of vortex core lines.

**Key words:** topological fluid dynamics, vortex dynamics

## 1. Introduction

Knots and links, as basic topological structural units (Adams 1994), play a fundamental and important role in various physical systems, such as hydrodynamics (Moffatt & Tsinober 1992; Kleckner & Irvine 2013; Moffatt 2021), plasma (Cirtain *et al.* 2013; Hao & Yang 2021), liquid crystal (Tkalec *et al.* 2011; Martinez *et al.* 2014), light field (Irvine

† Email address for correspondence: yyg@pku.edu.cn

& Bouwmeester 2008; Dennis *et al.* 2010) and DNA molecules (Wasserman & Cozzarelli 1986; Klotz, Soh & Doyle 2018).

In fluid systems knotted and linked vortex tubes are typical coherent structures (Ricca & Berger 1996), covering most scales in nature, from superfluid vortices at nanoscales (Barenghi 2007; Kleckner, Kauffman & Irvine 2016) to magnetic flux tubes at cosmic scales (Cirtain *et al.* 2013). In particular, the conceptual knotted and linked vortex tubes with complex topologies and geometries can be described as the 'sinews' of turbulence (Moffatt, Kida & Ohkitani 1994); tangled vortex tubes in homogeneous isotropic turbulence are analysed in Xiong & Yang (2019*b*).

The evolutionary topology and geometry of vortex knots and links can shed light on laminar-turbulent transition and energy cascade in turbulence (see Yao, Yang & Hussain 2021). The topological and geometric features are partly characterized by the helicity (Moreau 1961; Moffatt 1969) – an important conserved quantity in ideal flows. The detailed helicity dynamics is analysed using the conversion between writhing, linking and twisting helicity components (e.g. Kleckner & Irvine 2013; Scheeler *et al.* 2017; Yao *et al.* 2021).

The study of vortex knots and links started in ideal flows (Thomson 1878). Under the local induction approximation (LIA) (Hama 1962; Kida 1981), the self-induced motion of a vortex filament in an ideal flow can be characterized by the curve dynamics governed by the nonlinear Schrödinger equation (Betchov 1965; Hasimoto 1972). The LIA-based studies on vortex knots found the possible steady state (Kida 1981) and the topological preservation under periodic motion (Keener 1990).

The Biot–Savart (BS) law can achieve better long-term evolution estimates of vortex knots than the LIA (Ricca, Samuels & Barenghi 1999; Fuentes 2010). Ricca *et al.* (1999) used numerical simulations with the BS law to show that vortex torus knots either translate maintaining their shape or unfold immediately. Barenghi, Hänninen & Tsubota (2006) numerically solved the BS equation for coiled vortex loops with finite-amplitude Kelvin waves (Maxworthy 1977), and found that the loops remain stable and their forward speed can be reduced or even reversed at large torus aspect ratios. This finding is supported by the theoretical study of Oberti & Ricca (2019) and extended to various torus knots by incorporating the Moore–Saffman desingularization into the BS law.

In viscous flows vortex tubes can undergo topological transformation, such as reconnection (Melander & Hussain 1988; Kida, Takaoka & Hussain 1991; Kida & Takaoka 1994; Yao & Hussain 2020*a*, 2022) and merging (Griffiths & Hopfinger 1987; Melander, Zabusky & McWilliams 1988; Le Dizes & Verga 2002), which cannot be captured by the LIA or BS law.

Using direct numerical simulation (DNS) of the Navier–Stokes (NS) equations, Kida & Takaoka (1988, 1987) found that the trefoil vortex knots in viscous flows are untied into unknotted vortex loops via the 'bridging' reconnection, and the total helicity fluctuates after reconnection. Aref & Zawadzki (1991) demonstrated that two initially separated vortex loops could be linked in during evolution, indicating that the linking and writhing helicities can be converted into each other through reconnection.

Kleckner & Irvine (2013) experimentally created thin knotted and linked vortex tubes in a water tank, and found that the untying of vortex knots/links is associated with cross-scale helicity conversion from knotting and linking to coiling structures. Scheeler *et al.* (2014, 2017) analysed the writhing-to-twisting helicity conversion in the stretching and compression of coiled vortex loops. These experiments showed the preservation of the writhing helicity and the decay of the twisting helicity.

In recent numerical simulations, Kerr (2018*b*) investigated the topology and helicity transformation of interacting coiled loops, and Kerr (2018*c*) found that the helicity of a

disturbed trefoil vortex knot is initially conserved and decays after reconnection. Xiong & Yang (2019*a*, 2020) developed a method for constructing knotted/linked vortex tubes with arbitrary geometry and tunable twist. They found that the cinquefoil and septafoil vortex knots undergo secondary vortex reconnection and then evolve into a turbulent-like state, and their helicities decay rapidly during the breakup and coaxial interactions of pinched-off vortex rings. Zhao *et al.* (2021) found a helicity jump during the reconnection of trefoil knotted vortices at large Reynolds numbers. Zhao & Scalo (2021) further quantified the relation between the helicity growth and circulation transfer using the reconnection model of two infinitesimal antiparallel vortex filaments. Yao *et al.* (2021) revealed that large positive and negative twist helicities are simultaneously generated before and during the asymmetric vortex reconnection, and then both components decay at different rates, causing the transient growth of the total helicity at large Reynolds numbers. Kivotides & Leonard (2021) showed the conversion of the linking to writhing helicity in the reconnection of Hopf vortex links with the vortex filament method. In addition, numerical simulations of superfluid vortex knots (Proment, Onorato & Barenghi 2012; Kleckner *et al.* 2016) and links (Zuccher & Ricca 2017) also showed the unknotting process via reconnections.

On the other hand, most of the extensive studies on vortex knots and links are restricted to simple initial configurations, such as the trefoil knot and Hopf link, and limited helicity conversion mechanisms through reconnection and stretching/compression of vortex tubes. To explore possible elementary structures and simple model vortices in turbulence, we study the evolution of various vortex torus knots and links over a range of winding numbers and torus aspect ratios using the DNS in viscous flows. This provides a full scope of the knot/link evolution by searching all possible topological transition routes, and explores new mechanisms of helicity conversion. In particular, the feasible initial construction method of knotted/linked vortex tubes (Xiong & Yang 2020) facilitates this investigation.

The outline of this paper is as follows. The topological helicity decomposition, especially into coherent knotted fields is outlined in § 2. The initial configuration and numerical simulation set-up of knotted and linked vortex tubes are described in § 3. The stability of coiled vortex loops is studied in § 4, and the vortex and helicity dynamics of vortex torus knots and links is investigated in § 5. Some conclusions are drawn in § 6.

## 2. Helicity decomposition

### 2.1. *Closed vortex tubes*

The helicity

$$H = \iiint h \,\mathrm{d}\mathcal{V} \tag{2.1}$$

is the integral of the helicity density $h = \boldsymbol{u} \cdot \boldsymbol{\omega}$, the dot product of the fluid velocity $\boldsymbol{u}$ and the vorticity $\boldsymbol{\omega} = \boldsymbol{\nabla} \times \boldsymbol{u}$, over a domain bounded by a vortex surface (Moffatt 1969). We first consider a closed vortex tube whose centreline is a smooth closed curve. Moffatt & Ricca (1992) derives the relation

$$H = n_c \Gamma^2 = \Gamma^2 (W_r(\mathcal{C}) + T_w(\mathcal{R})) \tag{2.2}$$

between $H$ and the Călugăreanu–White invariant $n_c$, where $\Gamma$ denotes the strength of the vorticity flux along the centreline or vortex axis $\mathcal{C}$, and $n_c$ is a basic invariant of mathematical ribbons. By placing a ribbon $\mathcal{R}$ of edges $\mathcal{C}$ and $\mathcal{C}^*$ in the tube (see figure 1), $n_c$ can be further decomposed into two geometric quantities, i.e. the writhing number $W_r$ and the twist number $T_w$. Here, $W_r = W_r(\mathcal{C})$ is related only to the geometry of $\mathcal{C}$,

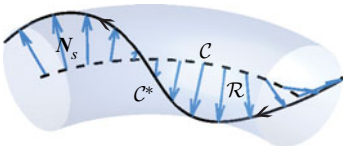


Figure 1. Schematic of a twisted vortex tube with finite twisting helicity. The dashed curve $\mathcal{C}$ represents the centreline of the vortex tube, and the solid curve line $\mathcal{C}^*$ denotes a twisted vortex line on the vortex tube, $\boldsymbol{N}_s$ denotes the radial unit vector from $\mathcal{C}$ to $\mathcal{C}^*$ and $\mathcal{R}$ denotes a ribbon with edges $\mathcal{C}$ and $\mathcal{C}^*$.

representing the contribution of bending or knotting of $\mathcal{C}$ to $H$, while $T_w = T_w(\mathcal{R})$ is the geometrical quantity of the virtual ribbon placed in the tube (see Fuller 1971), representing the contribution of twisting of the vorticity field to $H$.

The writhing number is calculated by

$$W_r = \frac{1}{4\pi} \oint_{\mathcal{C}} \oint_{\mathcal{C}} \frac{(\boldsymbol{x} - \boldsymbol{x}^*) \cdot \mathrm{d}\boldsymbol{x} \times \mathrm{d}\boldsymbol{x}^*}{|\boldsymbol{x} - \boldsymbol{x}^*|^3}, \tag{2.3}$$

where $\boldsymbol{x}$ and $\boldsymbol{x}^*$ denote two points on $\mathcal{C}$. The twisting number is calculated by

$$T_w = \frac{1}{2\pi} \oint_{\mathcal{C}} \left(\boldsymbol{N}_s \times \boldsymbol{N}_s'\right) \cdot \boldsymbol{T}\, \mathrm{d}s, \tag{2.4}$$

where $\boldsymbol{N}_s$ denotes a radial unit vector from $\mathcal{C}$ to $\mathcal{C}^*$ on $\mathcal{R}$, $\boldsymbol{N}_s' = \mathrm{d}\boldsymbol{N}_s/\mathrm{d}s$, $\boldsymbol{T}$ denotes the unit tangent vector of $\mathcal{C}$ and $s$ is the arc-length parameter.

The twisting number $T_w = T_t + T_i$ can be further geometrically decomposed into the total torsion

$$T_t(\mathcal{C}) = \frac{1}{2\pi} \oint_{\mathcal{C}} \tau(s)\, \mathrm{d}s, \tag{2.5}$$

which is only related to the centreline, and the intrinsic twist (Moffatt & Ricca 1992)

$$T_i(\mathcal{R}) = \frac{[\theta]_{\mathcal{R}}}{2\pi} = \frac{1}{2\pi} \oint_{\mathcal{C}} \xi(s)\, \mathrm{d}s, \tag{2.6}$$

which is determined by the azimuthal variation $[\theta]_{\mathcal{R}}$ of a vortex line. Here, $\tau$ is the torsion of the curve $\mathcal{C}$, and $\xi$ is the intrinsic rate of the azimuth change along $\mathcal{C}$. When the centreline passes through an inflection point where the curvature vanishes, $T_t(\mathcal{C})$ and $T_i(\mathcal{R})$ jump discontinuously through $\pm 1$ and $\mp 1$, respectively (Moffatt & Ricca 1992). Since the generation and elimination of the inflection point are common in the continuous deformation of $\mathcal{C}$ during the evolution of vortex tubes, it appears to be more suitable to use $T_w$ rather than $T_t$ to describe the internal twist of vortex lines within the vortex tube.

When multiple closed vortex tubes are linked to each other in the flow field, the topological decomposition of $H$ further introduces the Gauss linking number

$$L_{k,ij} = L_k(\mathcal{C}_i, \mathcal{C}_j) = \frac{1}{4\pi} \oint_{\mathcal{C}_i} \oint_{\mathcal{C}_j} \frac{\left(\boldsymbol{x}_i - \boldsymbol{x}_j\right) \cdot \mathrm{d}\boldsymbol{x}_i \times \mathrm{d}\boldsymbol{x}_j}{\left|\boldsymbol{x}_i - \boldsymbol{x}_j\right|^3} \tag{2.7}$$

between vortex tubes $i$ and $j$, where $\boldsymbol{x}_i$ and $\boldsymbol{x}_j$ denote points on $\mathcal{C}_i$ and $\mathcal{C}_j$, respectively. Thus, the full helicity decomposition (e.g. Berger & Field 1984; Scheeler *et al.* 2014) reads as

$$H = \sum_{i \neq j} \Gamma_i \Gamma_j L_{k,ij} + \sum_i \Gamma_i^2 (W_{r,i} + T_{w,i}), \tag{2.8}$$

where $\Gamma_i$, $W_{r,i}$ and $T_{w,i}$ are the circulation, writhing number and twisting number of vortex tube $i$, respectively.

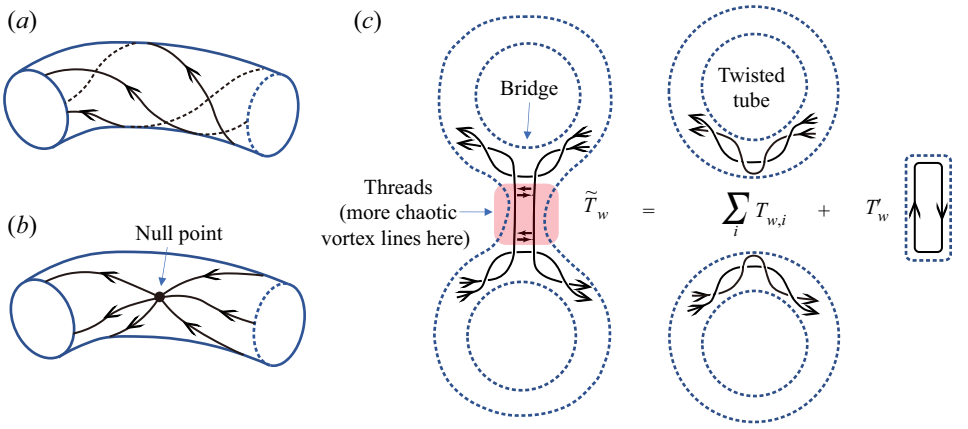


Figure 2. Schematics of vortex lines (black solid lines) integrated from the vorticity field with (*a*) no null point or (*b*) one null point on vortex surfaces. (*c*) Schematic for the generation of the generalized twist number during the bridging vortex reconnection, which is illustrated by a virtual surgery.

### 2.2. *Coherent knotted fields*

The above discussion is based on the ideal closed vortex tube constituting vortex lines lying on nested torus vortex surfaces. When the vortex tubes reconnect or merge, the helicity decomposition (2.8) may break down due to the significant topological change.

Take the viscous vortex reconnection of a trefoil knotted vortex tube for example (e.g. Kleckner & Irvine 2013; Yao *et al.* 2021; Zhao *et al.* 2021). In topology, the genus $g_v$ of the closed orientable surface that wraps the vortex changes from $g_v = 1$ for the initial trefoil knot to $g_v = 4$ for the interconnected structure during reconnection. After the reconnection is completed, the major vortical structure becomes two loops with $g_v = 1$. For a vortical structure with $g_v > 1$, the vorticity field must have one or more null points on the closed vortex surface based on the Poincaré–Hopf theorem (Milnor & Weaver 1997). As illustrated in figure 2(*a*,*b*), vortex lines originate or annihilate at the null point. Furthermore, the reconnection triggers scale cascade to produce small-scale structures such as bridges and threads. The convoluted structures above do not satisfy an important assumption in the decomposition of (2.8) – all vortex lines lie on a family of surfaces nested around the central closed curve (Chui & Moffatt 1995).

Thus, the exact helicity decomposition (2.8) is not applicable during the vortex reconnection, but a generalized helicity decomposition can still be useful to characterize geometric features of a coherent knotted field in which the vortex cores can be identified. After reconnection or merging of vortex tubes with the same circulation $\Gamma$, the vorticity is still concentrated in a large-scale tube-like structure. This coherent vortex structure can still be regarded as closed tubes, and each loop has a closed and smooth centreline and nearly constant circulation. The contribution of $W_r$ determined by the centreline to $H$ can be evaluated by (2.3). The remainder of the normalized total helicity can be defined as a generalized twist number (Yao *et al.* 2021)

$$\tilde{T}_w = \frac{H}{\Gamma^2} - \sum_i W_{r,i} - \sum_{i \neq j} L_{k,ij}. \tag{2.9}$$

We demonstrate that $\tilde{T}_w$ has a certain connection with $T_w$. As sketched on the left of figure 2(*c*), we consider a vortical structure with $g_v = 2$ formed in reconnection. Between the two large-scale vortex rings at the top and bottom, some vortex lines are wound from

one ring to the other through small-scale vortex tubes. We perform a virtual surgery on the vorticity field by cutting off the junction part and then adding two pairs of opposite vortex tubes. As sketched on the right of figure 2(*c*), the original structure is equivalent to two isolated vortex rings and an attached structure connecting the two rings and consisting of small-scale vortex tubes (e.g. threads). Therefore, the generalized twisting number can be re-expressed by

$$\tilde{T}_w = \sum_i T_{w,i} + T'_w, \tag{2.10}$$

where $\sum_i T_{w,i}$ is the sum of twisting contributions of the virtual large-scale vortex rings, and $T'_w$ represents the twisting contribution from all small structures attached to the main vortex tube. This generalized twisting number characterizes the degree of entanglement of the vorticity field. By replacing $T_w$ by $\tilde{T}_w$, the helicity decomposition (2.8) becomes

$$H = \Gamma^2 \left[ \sum_{i \neq j} L_{k,ij} + \sum_i (W_{r,i} + T_{w,i}) + T'_w \right]. \tag{2.11}$$

## 3. Simulation overview

### 3.1. *Torus knots and links*

In the present study the centreline $\mathcal{C}$ of vortex tubes is a torus unknot, knot or link $\mathcal{T}_{p,q}$. It is a discrete rotationally symmetric closed curve embedded on a two-dimensional torus $\Pi$ in $\mathbb{R}^3$. Namely, it has $q$-fold symmetry about the rotational symmetry axis of $\Pi$. The curve $\mathcal{C}$ characterized by the integer pair $(p, q)$ winds $q$ times around a circle in the interior of $\Pi$, and $p$ times around its axis of rotational symmetry. The ratio $w = |q/p|$ is the winding number, a measure of the knot and link topology (Oberti & Ricca 2016). Each $\mathcal{T}_{p,q}$ is specified by a pair of integers $p$ and $q$. If $p$ and $q$ are co-prime, $\mathcal{T}_{p,q}$ is an isolated torus knot. If $|p| \leqslant 1$ or $|q| \leqslant 1$, $\mathcal{T}_{p,q}$ is an unknot which is ambient isotopic to a standard circle in topology. If $p$ and $q$ are not relatively prime, $\mathcal{T}_{p,q}$ is a torus link with $n$ components $\mathcal{T}_{p/n,q/n}$, where $n$ is the greatest common divisor of $p$ and $q$.

The parametric equation $\boldsymbol{c}(\zeta) = (c_x(\zeta), c_y(\zeta), c_z(\zeta))$ of torus knots or unknots is

$$\left.\begin{aligned} c_x(\zeta) &= R_t\,(1 + \lambda\cos(q\zeta))\cos(p\zeta), \\ c_y(\zeta) &= R_t\,(1 + \lambda\cos(q\zeta))\sin(p\zeta), \quad \zeta \in [0, 2\pi), \\ c_z(\zeta) &= -R_t\lambda\sin(q\zeta), \end{aligned}\right\} \tag{3.1}$$

where $\lambda = r_t/R_t \in [0, 1)$ denotes the torus aspect ratio, and $R_t$ and $r_t$ are the major and minor radii of $\Pi$, respectively. Figure 3 illustrates three $\mathcal{T}_{1,6}$ embedded on $\Pi$ with different $\lambda$. The winding amplitude of $\mathcal{C}$ grows with $\lambda$ and vanishes for a standard circle with $\lambda = 0$.

Each component $\mathcal{T}_{p/n,q/n}$ of a torus link is a torus knot or unknot. Its parametric equation is

$$\left.\begin{aligned} c_x(\zeta) &= R_t\,(1 + \lambda\cos(q\zeta/n))\cos(p\zeta/n), \\ c_y(\zeta) &= R_t\,(1 + \lambda\cos(q\zeta/n))\sin(p\zeta/n), \quad \zeta \in [0, 2\pi), \\ c_z(\zeta) &= -R_t\lambda\sin(q\zeta/n). \end{aligned}\right\} \tag{3.2}$$

The rest of the link components are determined by rotating the curve (3.2) clockwise around the axis of rotational symmetry by $2\pi/q$. Figure 4 depicts the torus unknot $\mathcal{T}_{1,3}$, torus knot $\mathcal{T}_{2,3}$ and torus link $\mathcal{T}_{2,4}$ embedded on the same $\Pi$ of $\lambda = 0.5$. In this study

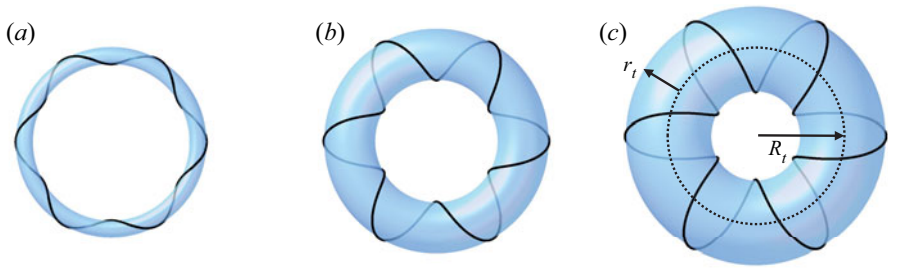


Figure 3. Diagram of torus unknot $\mathcal{T}_{1,6}$ with (*a*) $\lambda = 0.1$, (*b*) $\lambda = 0.3$ and (*c*) $\lambda = 0.5$. Black curves denote different torus unknots $\mathcal{C}$, and blue surfaces denote the torus $\Pi$ with the same $R_t$ and different $\lambda$.

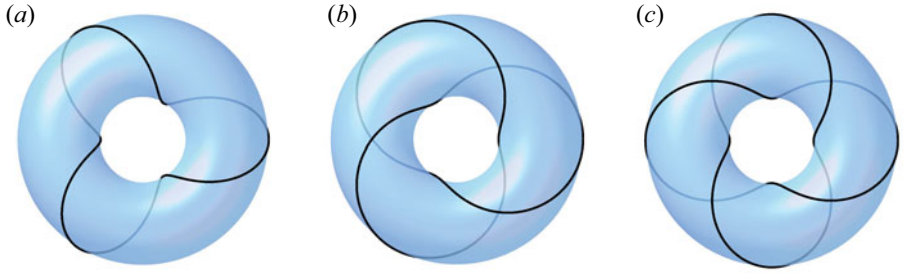


Figure 4. Diagram of torus (*a*) unknot $\mathcal{T}_{1,3}$, (*b*) knot $\mathcal{T}_{2,3}$ and (*c*) link $\mathcal{T}_{2,4}$. Black curves denote different torus unknots $\mathcal{C}$, and blue surfaces denote the torus $\Pi$ with the same $R_t$ and different $\lambda$.

we consider positive integer pairs $(p, q)$, and set constant $R_t = \sqrt{2}/2$. This choice of $R_t$ is to avoid the vortex touching the boundary at late times for large $R_t$ and to have self-intersection at early times for small $R_t$. Note that $\mathcal{T}_{p,-q}$ is the mirror image of $\mathcal{T}_{p,q}$. Thus, the topology and geometry of $\mathcal{T}_{p,q}$ are characterized by three parameters $p$, $q$ and $\lambda$.

### 3.2. *Initial configuration of vortex tubes*

Based on the parametric equation (3.1) or (3.2) of the vortex centerline and the curved cylindrical coordinate system $(s, \rho, \theta)$, we specify the vorticity of the vortex tube as (see Xiong & Yang 2020)

$$\boldsymbol{\omega}(s, \rho, \theta) = \Gamma f(\rho)\left[\boldsymbol{e}_s + \frac{\rho\eta}{1 - \kappa\rho\cos\theta}\boldsymbol{e}_\theta\right], \tag{3.3}$$

where the circulation $\Gamma$ of the initial vortex tube is set to be $\Gamma_0 = 1$, the vorticity distribution

$$f(\rho) = \frac{1}{2\pi\sigma^2}\exp\left(-\frac{\rho^2}{2\sigma^2}\right) \tag{3.4}$$

is a Gaussian function with the standard deviation $\sigma = \sigma_0 = 1/(16\sqrt{2\pi}) \approx 0.025$, where $\boldsymbol{e}_s$ and $\boldsymbol{e}_\theta$ are the axial and azimuthal unit vectors, respectively, $\kappa$ is the curvature of $\mathcal{C}$ and $\eta(s) = \tau(s) + \xi(s) = (\boldsymbol{N}_s \times \boldsymbol{N}_s') \cdot \boldsymbol{T}$ denotes the local twist rate of the vortex tube.

| Numerical simulations | $r_c/\bar{R}$ | $L/\bar{R}$ |
|---|---|---|
| Present DNS | 0.071 | 8.89 |
| Kerr (2018*a*) | 0.1, 0.2 | 6.28 |
| Kerr (2018*b*) | 0.18, 0.3 | 3.77, 6.28 |
| Xiong & Yang (2019*a*) | 0.1 | 6.28 |
| Zhao *et al.* (2021) | 0.059 | 13.33, 6.67 |
| Zhao & Scalo (2021) | 0.059, 0.119, 0.178, 0.237 | 13.04 |
| Yao *et al.* (2021) | 0.05 | 6.28 |

Table 1. Comparison of vortex tube thicknesses and simulation box sizes in the present and recent numerical simulations.

Note that $\eta$, the integrand in the definition of $T_w$ in (2.4), is constant for a uniformly twisted vortex tube, so that the twisting number can be tuned by varying

$$\eta = \frac{2\pi T_w}{l_c}, \tag{3.5}$$

where $l_c$ denotes the length of $\mathcal{C}$. In this study the initial vortex tubes have $T_w = 0$ by setting $\eta = 0$ with $\xi(s) = -\tau(s)$, which ensures that all vortex lines are initially parallel to $\mathcal{C}$ everywhere.

The vortex tube thickness can be characterized by $\sigma$ in (3.4), the Lamb–Oseen core size $a$ or the vortex core radius $r_c$, with the relation $r_c^2 = 2a^2 = 4\sigma^2$ (Zhao & Scalo 2021). In the present study the ratio between $r_c$ and the vortex average radius

$$\bar{R}(t) = \frac{1}{l_c} \oint_{\mathcal{C}} R(s)\, \mathrm{d}s \tag{3.6}$$

is set to be $r_c/\bar{R} = 0.071$, where $R(s)$ is the distance between a point on $\mathcal{C}$ and the $q$-fold rotational symmetry axis of $\Pi$. The corresponding vortex tube is relatively thin, compared with those in recent numerical simulations in table 1.

In the numerical implementation, (3.3) is specified in a periodic box with dimensions $(2\pi)^3$ in terms of Cartesian coordinates via the numerical algorithm transforming $\boldsymbol{x}$ into $(s, \rho, \theta)$ of Xiong & Yang (2020). This numerical construction has been demonstrated to be very robust to generate a smooth vorticity field even for the thick vortex tube with self-intersection (Xiong & Yang 2019*a*). The velocity is calculated from the vorticity via the BS law in Fourier space

$$\boldsymbol{u} = \mathcal{F}^{-1}\left(\frac{i\boldsymbol{k} \times \hat{\boldsymbol{\omega}}}{|\boldsymbol{k}|^2}\right), \tag{3.7}$$

where $\mathcal{F}^{-1}$ denotes the inverse Fourier transform, $\boldsymbol{k}$ denotes the wavenumber in Fourier space, and $\hat{\boldsymbol{\omega}} = \mathcal{F}(\boldsymbol{\omega})$ denotes the Fourier coefficient of $\boldsymbol{\omega}$ with the Fourier transform $\mathcal{F}$.

### 3.3. *Direct numerical simulation*

We take the velocity fields of vortex torus knots/links as initial conditions and calculate each evolution using DNS. The velocity field $\boldsymbol{u}(\boldsymbol{x}, t)$ of an incompressible viscous flow

| $p$ | 1 | 1 | 1 | 1 | 1 | 2 | 2 | 2 | 2 |
|---|---|---|---|---|---|---|---|---|---|
| $q$ | $1\sim6$ | $1\sim6$ | $1\sim6$ | $1\sim6$ | 12 | 3 | $1, 2, 4\sim6$ | $1\sim6$ | 3 |
| $\lambda$ | 0.1 | 0.3 | 0.5 | 0.7 | 0.5 | 0.1 | 0.1 | 0.5 | 0.3 |
| $N$ | 512 | 512 | 512 | 512 | 2048 | 1024 | 512 | 512 | 1024 |
| $k_{max}\eta_K$ | 2.97 | 2.58 | 2.31 | 2.14 | 7.27 | 5.20 | 2.57 | 2.23 | 5.09 |

Table 2. Direct numerical simulation parameters: integers $p$ and $q$ for characterizing a torus knot/link, the torus aspect ratio $\lambda$, the number of grid points $N$ and the spatial resolution $k_{max}\eta_K$.

with constant unit density is governed by the NS equations

$$\left.\begin{aligned}\frac{\partial \boldsymbol{u}}{\partial t}+(\boldsymbol{u}\cdot\boldsymbol{\nabla})\boldsymbol{u}&=-\boldsymbol{\nabla}p+\nu\nabla^2\boldsymbol{u},\\ \boldsymbol{\nabla}\cdot\boldsymbol{u}&=0,\end{aligned}\right\}\tag{3.8}$$

where $t$ denotes the time, $p$ the pressure and $\nu$ the kinematic viscosity.

The DNS for (3.8) is performed in the periodic box of side $L=2\pi$ with $N^3$ uniform grid points using a standard pseudo-spectral method. Here, the DNS box size should be much larger than the vortex average radius, i.e. $L\gg\bar{R}$, to avoid numerical artifacts due to periodic boundary conditions. Zhao *et al.* (2021) argued and validated that $L/\bar{R}=6.67$ is large enough. As listed in table 1, $L/\bar{R}=8.89$ is used in the present study, which satisfies the criterion suggested by Zhao *et al.* (2021) and is relatively large in the current studies. Note that Zhao *et al.* (2021) and Zhao & Scalo (2021) utilized a compressible flow solver with the block-structured adaptive mesh refinement and the high-order compact finite difference scheme to achieve smaller $r_c/\bar{R}$ and larger $L/\bar{R}$ in the simulation of vortex knots than those in the present and other previous studies. The numerical solver removes aliasing errors using the two-third truncation method with the maximum wavenumber $k_{max}\approx N/3$. The Fourier coefficient of $\boldsymbol{u}$ is advanced in time by a second-order Adams–Bashforth scheme. The time step is chosen to ensure the Courant–Friedrichs–Lewy number is less than 0.5 for numerical stability and accuracy. This numerical solver has been used and validated in various applications (e.g. Yang, Pullin & Bermejo-Moreno 2010; Zheng, You & Yang 2017; Xiong & Yang 2019*a*). A non-dimensionalized time $t^*=t/(R_t^2/\Gamma_0)$ is used in post-processing.

We carry out a series of DNS at the vortex Reynolds number $Re\equiv\Gamma_0/\nu=2000$ with various $p$, $q$, $\lambda$ and $N$, which are listed in table 2. To ensure that the grid resolution can fully resolve the flow evolution, $N$ is carefully chosen to be from 512 to 2048 for different cases. A grid convergence test is detailed in Appendix A, including a typical reconnection case of the trefoil knot and a transition case with highly intensive vortex interactions. Considering that the flow evolutions in over a half of cases have bridging reconnections or evolve into a turbulent-like state, we also list the lowest spatial resolution $k_{max}\eta_K$ for the DNS cases in the entire evolution in table 2 for reference, where $\eta_K=(\nu^3/\varepsilon)^{1/4}$ denotes the Kolmogorov length scale, and $k_{max}\eta_K$ is always greater than 2 in the temporal evolution, satisfying the criterion $k_{max}\eta_K\geqslant1.5$ (Pope 2000) for resolving the smallest scales in turbulence.

## 4. Evolution of coiled vortex loops $\mathcal{T}_{1,q}$

### 4.1. *Effects of the torus aspect ratio*

The evolution of a slender closed vortex tube with a specified thickness is generally determined by its centreline geometry, which is fully characterized by the integer pair $(p, q)$ and torus aspect ratio $\lambda$ in (3.1) or (3.2). Given the large parametric space of $p$, $q$ and $\lambda$, we first consider the vortex torus unknot $\mathcal{T}_{1,q}$ with the winding number $w = q$. It is a coiled vortex loop with different degrees of winding structure for different $q$ and $\lambda$.

We take vortex $\mathcal{T}_{1,3}$ as an example to illustrate the effect of $\lambda$ on the vortex centreline geometry and evolution. Figure 5 shows the initial configuration and the temporal evolution of $\mathcal{T}_{1,3}$ with $\lambda = 0.1$, 0.3, 0.5 and 0.7 using the isosurface of $|\boldsymbol{\omega}| = 0.04\omega_0$ colour-coded by the helicity density $h$, where $\omega_0$ denotes the maximum initial vorticity magnitude.

Note that the isosurface of $|\boldsymbol{\omega}| = 0.04\omega_0$ contains 96 % of the circulation at the initial time. Its isocontour threshold is selected after tuning to identify the major vortical structures and distinguish signature stages in the temporal evolution of vortex loops, because in general, very thin or weak threads are not captured for too large thresholds (e.g. $|\boldsymbol{\omega}| > 0.1\omega_0$), and the fine structures are merged into a bulky one for too small thresholds (e.g. $|\boldsymbol{\omega}| < 0.01\omega_0$). We find that most geometric and topological features of vortical structures can be identified within a small range of isocontour values $0.01\omega_0 \leq |\boldsymbol{\omega}| \leq 0.1\omega_0$ at $t^* \leq 10$.

The vortex shape remains almost unchanged for small $\lambda = 0.1$, and the vortex deformation becomes notable with increasing $\lambda$. For $\lambda = 0.3$ and 0.5, three petal-like branches form and then relax via self-induction to a state close to the original shape. In addition to the overall movement along the $z$-axis as for ordinary vortex rings, these coiled vortex loops rotate counterclockwise around the axis of discrete rotational symmetry from the top view, and the rotational angular velocity grows with $\lambda$. For large $\lambda = 0.7$, the three petals are stretched with time, and then their tips are pinched off via the viscous vortex reconnection. Moreover, the evolution of coiled vortex loops can be affected by the vortex tube thickness and the Reynolds number – discussed in Appendices B and C.

Figure 6 shows the perspective and the close-up top views of vortex $\mathcal{T}_{1,3}$ for $\lambda = 0.7$ before and after the reconnection at $t^* = 6.5$ and 7.5, respectively. Before reconnection, a pair of vortex tubes near the 'neck' of each petal approach each other into an antiparallel state. Then, the antiparallel parts are reconnected under the bridging mechanism (Melander & Hussain 1988; Kida & Takaoka 1991), forming a structure with complex topology and genus $g_v > 1$. After the reconnection, a secondary vortex ring pinches off from each petal, and the central main part returns to a vortex loop of $\mathcal{T}_{1,3}$ with a smaller $\lambda$. Moreover, some small-scale threads connecting the central vortex loop and the three small secondary rings are stretched and gradually dissipated.

By comparing the evolution of vortices $\mathcal{T}_{1,3}$ with $\lambda = 0.5$ and 0.7, a minimum critical torus aspect ratio $\lambda_c$ seems to exist for triggering the vortex reconnection. In the approximation of the vortex filament, the motion of a vortex tube is determined by the BS law and the geometry of the vortex core line. We use the method based on the normalized helicity density (Levy, Degani & Seginer 1990) to extract the vortex core line $\mathcal{C}(t)$ from DNS data. This method was also applied to study the dynamics of a trefoil vortex knot (Yao *et al.* 2021).

Figure 7 depicts different temporal evolutions of the location and velocity of $\mathcal{C}(t)$ for $\lambda = 0.5$ and 0.7, where the arrow length is proportional to the local speed. For vortex $\mathcal{T}_{1,3}$ with $\lambda = 0.5$, the induction velocity on the core line stretches the petal-like branch at early times. The approaching speed of branch sides gradually decreases due to the reduced

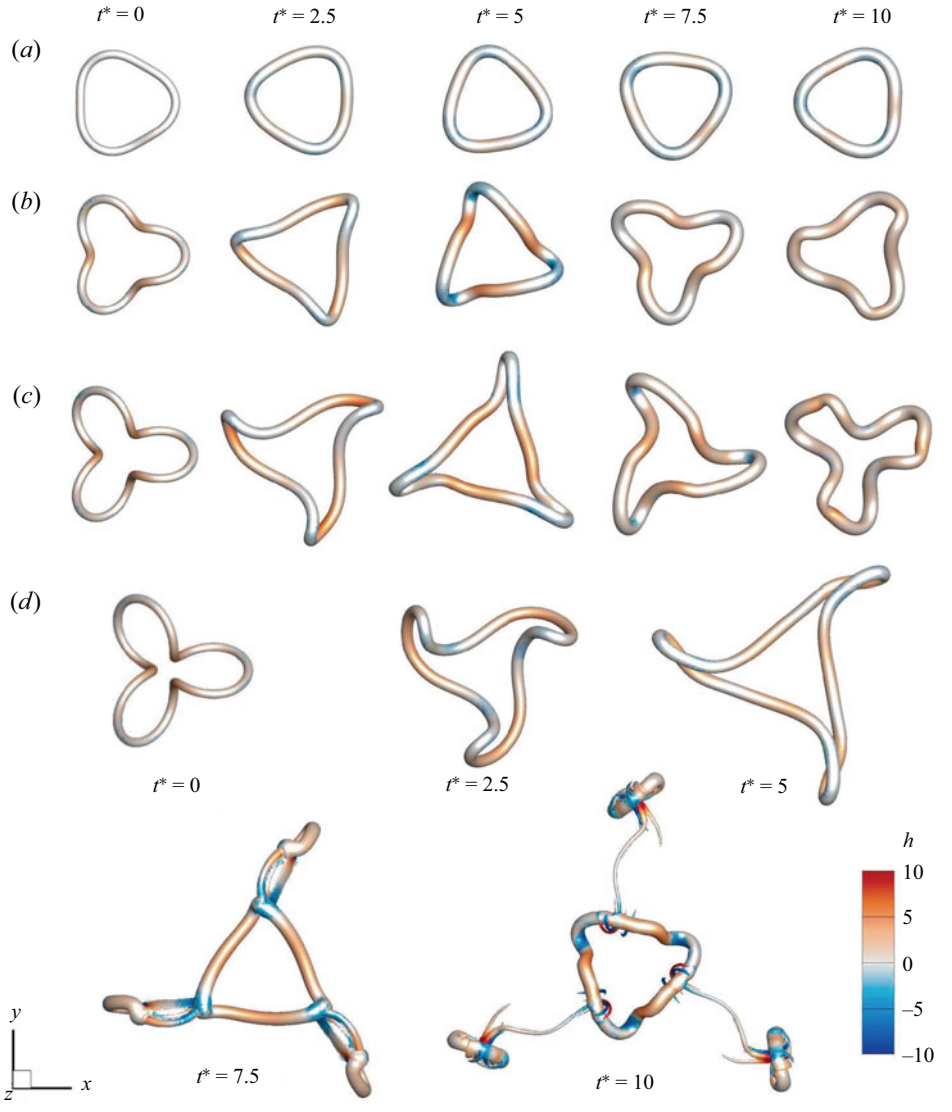


Figure 5. Evolution of the isosurface of $|\boldsymbol{\omega}| = 0.04\omega_0$ for vortex $\mathcal{T}_{1,3}$ with (*a*) $\lambda = 0.1$, (*b*) $\lambda = 0.3$, (*c*) $\lambda = 0.5$ and (*d*) $\lambda = 0.7$ at $t^* = 0, 2.5, 5, 7.5$ and 10 (from left to right). Surfaces are colour-coded by the helicity density. For vortex $\mathcal{T}_{1,3}$ with $\lambda = 0.7$ at $t^* = 10$, the central loop has $|\boldsymbol{\omega}|_{max} = 34.35$ and $\Gamma = 1.00$, and the secondary loop has $|\boldsymbol{\omega}|_{max} = 45.70$ and $\Gamma = 1.06$.

curvature in LIA-induced stretching, and then local vortex tubes repel each other as a relaxation process at late times. For $\lambda = 0.7$, by contrast, the local vortex tubes on two sides of the branch keep approaching each other to trigger the antiparallel reconnection.

We quantify the global geometry of $\mathcal{C}(t)$ by the average radius $\bar{R}(t)$, average torus aspect ratio

$$\bar{\lambda}(t) = \frac{R_{max} - R_{min}}{2\bar{R}} \tag{4.1}$$

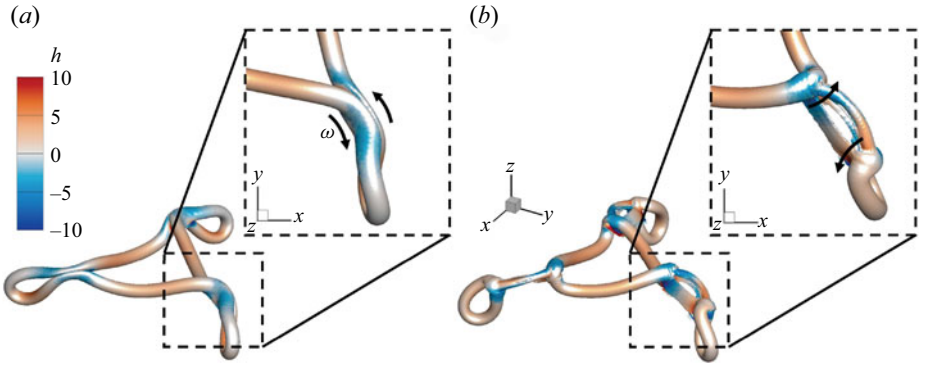


Figure 6. Close-up view of the isosurface of $|\boldsymbol{\omega}| = 0.04\omega_0$ for vortex $\mathcal{T}_{1,3}$ with $\lambda = 0.7$ at (*a*) $t^* = 6.5$ and (*b*) $t^* = 7.5$. The surfaces are colour-coded by the helicity density. The black arrow indicates the direction of the vorticity of the large-scale vortex tube.

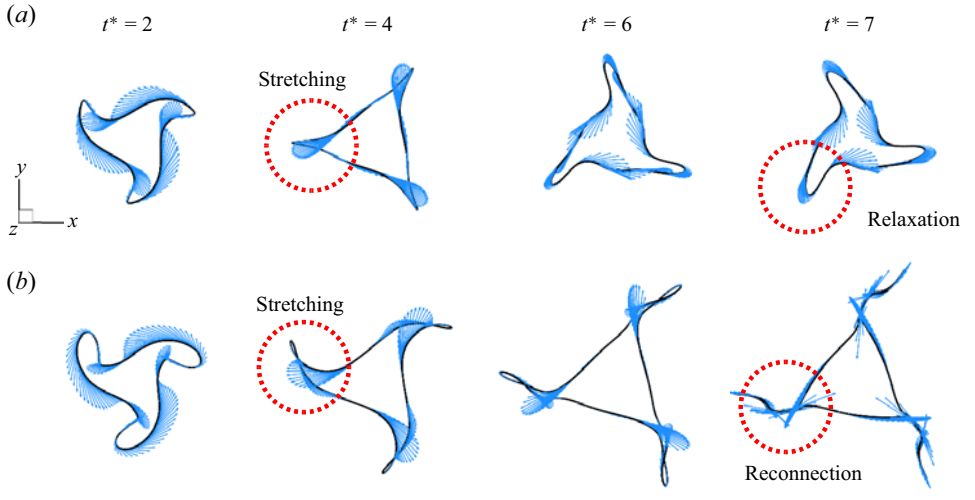


Figure 7. Local velocity on the vortex core line for vortex $\mathcal{T}_{1,3}$ with (*a*) $\lambda = 0.5$ and (*b*) $\lambda = 0.7$ at $t^* = 2$, 4, 6 and 7. The arrow length is proportional to the local speed.

and average $z$-coordinate

$$\bar{z}(t) = \frac{1}{l_c} \oint_{\mathcal{C}} z(s)\, \mathrm{d}s. \tag{4.2}$$

As illustrated in figure 8, $R_{max}$ and $R_{min}$ are the maximum and minimum values of $R(s)$, respectively. Figure 9 plots the time evolution of $\bar{\lambda}(t)$, $\bar{z}(t)$ and $\bar{R}(t)$ of vortex $\mathcal{T}_{1,3}$ with $\lambda = 0.1$, 0.3, 0.5 and 0.7, where the error bars denote the range between maximum and minimum values of $R(t)$ or $z(t)$ at a particular time; the $\lambda = 0.7$ case only considers the central secondary ring after reconnection for $t^* > 7$.

The evolution of $\bar{R}(t)$ in figure 9(*a*) shows that the average radius for $\lambda = 0.1$ remains unchanged with the preservation of the geometric shape. For $\lambda = 0.3$ and 0.5, $\bar{R}$ first increases and then decreases, corresponding to the stretching and relaxation processes in the $x$–$y$ plane in figure 7, respectively. For $\lambda = 0.7$, the branches are highly stretched, and $\bar{R}$ grows faster than that in lower $\lambda$ cases under self-induced motion. Then, the vortex

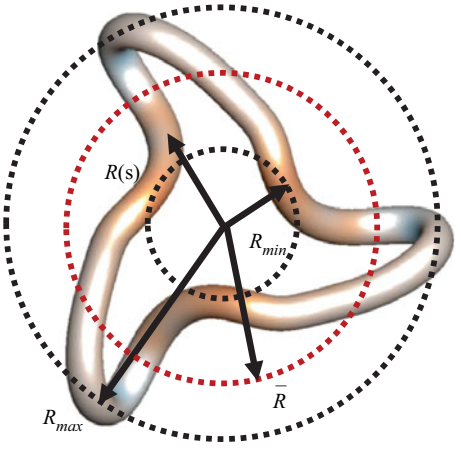


Figure 8. Illustration of $R_{max}$, $R_{min}$ and $\bar{R}$ of vortex $\mathcal{T}_{1,3}$ with $\lambda = 0.5$ at $t^* = 7.5$.

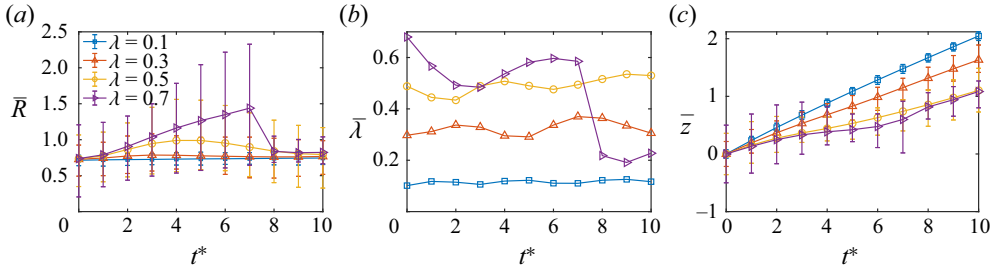


Figure 9. Evolution of (*a*) $\bar{R}(t)$, (*b*) $\bar{\lambda}(t)$ and (*c*) $\bar{z}(t)$ of vortex $\mathcal{T}_{1,3}$ with $\lambda = 0.1$, 0.3, 0.5 and 0.7, where the $\lambda = 0.7$ case only considers the central ring after reconnection for $t > 7$. Error bars denote the range between minimum and maximum values.

reconnection occurs, leaving a central secondary loop with a smaller $\bar{R}$, so the growth $\bar{R}$ is suddenly terminated.

The evolution of $\bar{\lambda}$ in figure 9(*b*) characterizes the winding amplitude of vortex loops (also see figure 3). For vortex loops with small initial $\lambda$ (= 0.1, 0.3 and 0.5), the variation of $\bar{\lambda}$ is generally small and quasi-periodic, so their evolution is stable. Here, the (Lyapunov) 'stability' of a vortex structure is defined in Ricca *et al.* (1999). If the vortex conserves topology, geometric signature (e.g. $p$, $q$ and $\bar{\lambda}$) and vortex coherency after travelling a considerable distance (much larger than their typical size) for some finite time, it is 'stable'. If the vortex breaks up or unfolds in a short time (compared with the typical time scale), it is 'unstable'. For $\lambda = 0.7$, $\bar{\lambda}(t)$ experiences large fluctuations in the early stage, and then it drops after the reconnection, because the central part of $\mathcal{T}_{1,3}$ becomes a vortex loop with a smaller $\lambda \approx 0.2$ (also see figure 5*d*).

The dominant motion of vortex loops is moving along the $z$-axis. The evolution of $\bar{z}$ in figure 9(*c*) shows the position and speed of $\mathcal{T}_{1,3}$ moving forward. The vortex loops without reconnection for $\lambda = 0.1$, 0.3 and 0.5 move at a constant speed, and the forward speed decreases with the increase of $\lambda$ (Barenghi *et al.* 2006; Oberti & Ricca 2019). For $\lambda = 0.7$, the vortex forward motion accelerates after the reconnection around $t^* = 7$, because the central loop is converted into the secondary one with a lower $\bar{\lambda}$, which has a faster forward speed. The range of $\bar{z}$ decreases before the reconnection, implying that the vortex tubes are approaching each other.

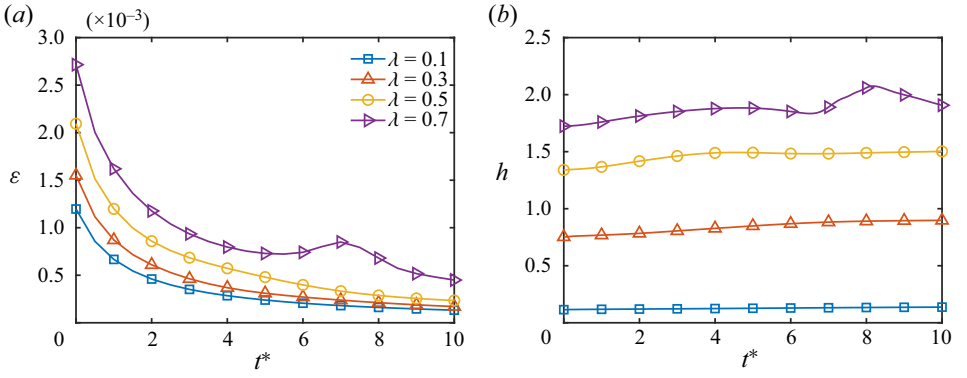


Figure 10. Evolution of (*a*) the mean dissipation rate and (*b*) total helicity for vortex $\mathcal{T}_{1,3}$ with $\lambda = 0.1$, 0.3, 0.5 and 0.7.

The results above suggest that the unstable vortex torus unknot with a larger initial torus aspect ratio tends to be transformed into a more stable one with a lower torus aspect ratio through the vortex reconnection.

In addition, the maximum vorticity magnitude $|\boldsymbol{\omega}|_{max}$ of the central parent loop or secondary offspring loops for $\mathcal{T}_{1,3}$ with $\lambda = 0.7$ at $t^* = 10$ are calculated in a subdomain surrounding each of them. As listed in the caption of figure 5, $|\boldsymbol{\omega}|_{max}$ of the central and secondary loops are different. The non-uniform $|\boldsymbol{\omega}|$ along the vortex axis during and after reconnection is caused by deformation of the local vortex core and twisting of vortex tubes. The circulations of the central and secondary loops are calculated in the $x$–$z$ plane at $y = \pi$ and the $x$–$y$ plane at $z = \bar{z}(t^* = 10)$, respectively. The circulation is almost conserved during the reconnection, which is consistent with the finding in Zhao & Scalo (2021) and supports the helicity decomposition in (2.9).

### 4.2. *Flow statistics and helicity analysis*

The geometric and topological changes of vortex loops alter the main flow statistics. Due to the viscous dissipation, the total energy $E_{tot} = \sum_k |\hat{\boldsymbol{u}}|^2/2$ of all cases decreases monotonically (not shown). In general, the mean dissipation rate $\varepsilon = \nu \sum_k (|\boldsymbol{k}|\,|\hat{\boldsymbol{u}}|)^2$ decays and the total helicity $H$ is almost conserved for $\lambda = 0.1$, 0.3 and 0.5 in figure 10. By contrast, we observe a bump of $\varepsilon$ and a transient growth of $H$ around $t^* = 7$ due to the vortex reconnection in the case of $\lambda = 0.7$, similar to the observations during reconnection of other vortex knots in (e.g. Xiong & Yang 2019*a*). The notable variations of $\varepsilon$ and $H$ are expected to be more significant for larger *Re* (see Yao *et al.* 2021; Zhao *et al.* 2021).

In order to elucidate the large helicity fluctuation during the bridging reconnection sketched in figure 2(*c*), we apply the positive–negative helicity decomposition $H^{\pm} = \int_{\mathcal{V}} h^{\pm}\,\mathrm{d}\mathcal{V}$ with

$$h^{+} = \begin{cases} h, & \text{if } h \geqslant 0, \\ 0, & \text{otherwise}, \end{cases} \tag{4.3}$$

and $h^{-} = h - h^{+}$, and the topological decomposition (2.11) to the case of $\lambda = 0.7$.

In figure 11(*a*) both $|H^{+}|$ and $|H^{-}|$ surge at $t^* = 6 \sim 8$, and the growth of $|H^{+}|$ is slightly larger than $|H^{-}|$ due to the asymmetric configuration during reconnection. The uneven growths cause the transient growth of $H$, which is also reported in Yao *et al.* (2021). After the reconnection, we simplify (2.11) by summing $W_r = \sum_i W_{r,i}$ and neglecting the

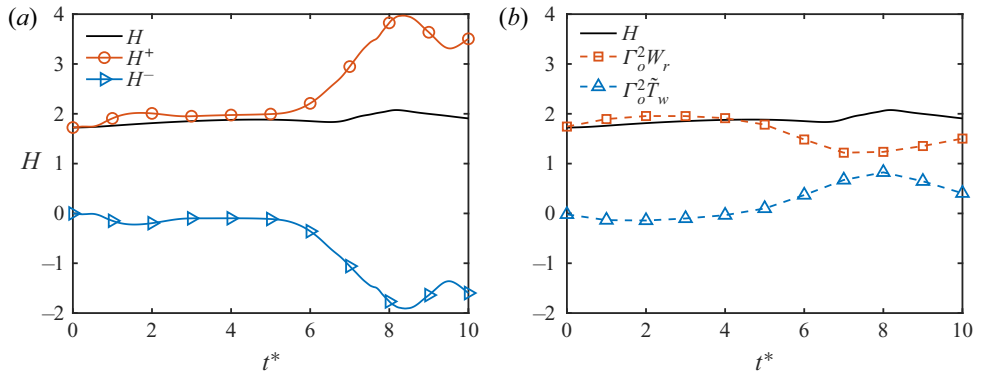


Figure 11. (*a*) Positive–negative and (*b*) topological decompositions of the total helicity of vortex $\mathcal{T}_{1,3}$ with $\lambda = 0.7$.

total Gauss linking number as $L_k = 0$, so the generalized twisting number becomes

$$\tilde{T}_w = H/\Gamma^2 - W_r. \tag{4.4}$$

Figure 11(*b*) shows $W_r$ and $\tilde{T}_w$ are almost conserved before reconnection. The conservation of $W_r$ for the evolution of vortex tubes without self-intersection is discussed in Appendix D. Then, $W_r$ is converted into $\tilde{T}_w$ during the reconnection, consistent with the finding for trefoil vortex knots (Yao *et al.* 2021; Zhao *et al.* 2021).

### 4.3. *Stability diagram of coiled vortex loops*

This subsection presents a systematic study on the effect of the torus aspect ratio on the stability (Ricca *et al.* 1999) of coiled vortex loops $\mathcal{T}_{1,q}$, extending the investigation in § 4.1. Note that $\mathcal{T}_{1,q}$ has been found as an intermediate or final topological state in the evolution of complex vortex knots (Scheeler *et al.* 2014; Kleckner *et al.* 2016; Xiong & Yang 2019*a*; Liu, Ricca & Li 2020).

For the coiled vortex loops $\mathcal{T}_{1,q}$, $q$ and $\lambda$ constitute the full geometric parameter space. We carried out DNS for 24 vortex torus unknots $\mathcal{T}_{1,q}$ with $q = 1 \sim 6$ and $\lambda = 0.1$, 0.3, 0.5 and 0.7. These coiled loops at $t^* = 0$ and 10 are visualized in figures 12(*a*) and 12(*b*), respectively. In the vortex evolution, we find that the coiled loops remain stable for smaller $q$ and $\lambda$, but break up into a central loop and $q$ small secondary loops for large $q$ and $\lambda$.

The deformation velocity of the vortex core line depends on the curvature according to the LIA (Hama 1962; Kida 1981). With the increase of $q$ and $\lambda$, the vortex loop becomes more coiled and experiences more severe deformation in the evolution. The vortex reconnection occurs as the initial $\lambda$ of vortex $\mathcal{T}_{1,q}$ exceeds a critical value $\lambda_c(q)$. The critical $\lambda_c(q)$ decreases with the increase of $q$; e.g. we observe $\lambda_c > 0.5$ for $q \leq 3$ and $0.3 < \lambda < 0.5$ for $4 \leq q \leq 6$ from reconnection events of $\mathcal{T}_{1,q}$ in figure 12(*b*).

Next, we focus on the cases of $\lambda = 0.3$ and 0.5 and $q = 4$, 5 and 6 close to the borderline cases with or without reconnection. For $\lambda = 0.3$, a cycle of stretching and relaxation processes maintains the relative stability of vortices $\mathcal{T}_{1,4}$ and $\mathcal{T}_{1,6}$ in figure 13(*a*,*b*). For $\lambda = 0.5$, the persistent stretching causes the reconnection of a pair of local vortex tubes with antiparallel vorticity directions for $\mathcal{T}_{1,4}$ and $\mathcal{T}_{1,6}$ in figure 13(*c*,*d*). The initial loop splits into $q$ small secondary loops moving outwards and leaving a coiled loop in the centre with smaller $\lambda$. The vortex reconnection for $\lambda = 0.5$ can be further quantified by the transient growth of $\varepsilon$ and $H$ observed in figure 14. The reconnection occurs earlier

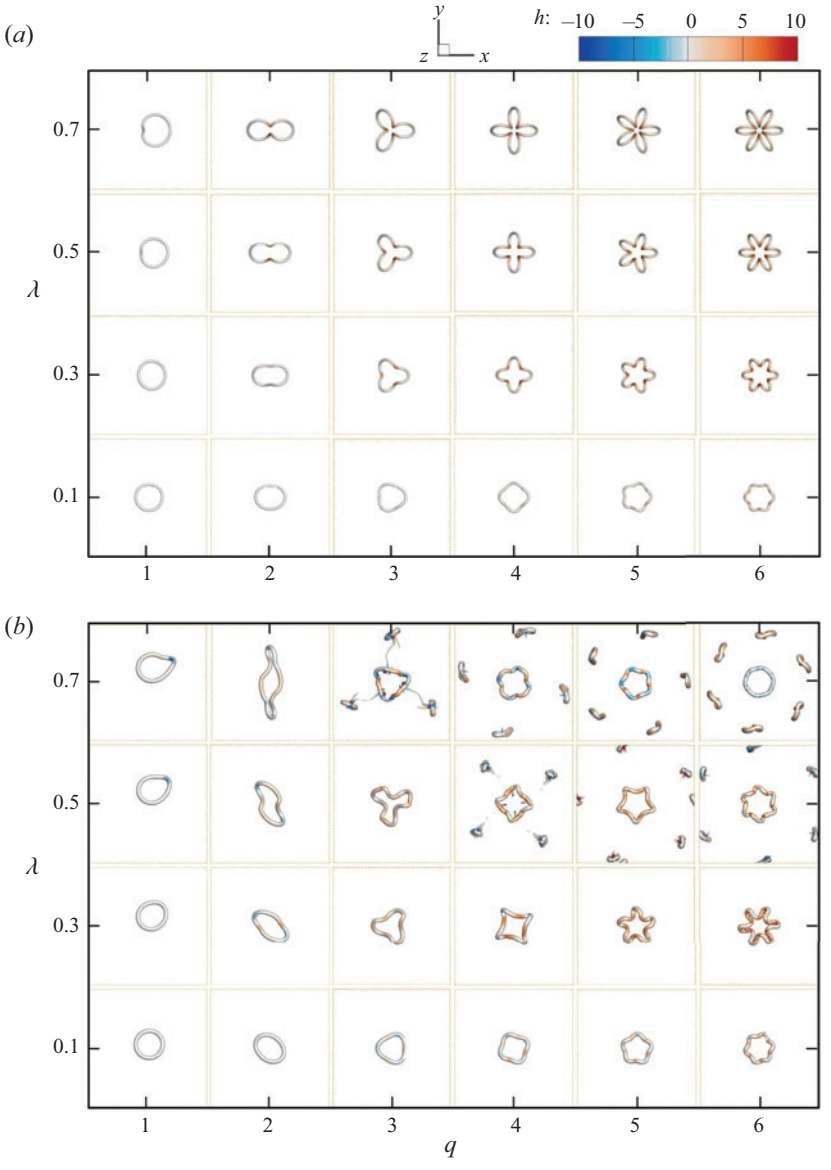


Figure 12. Coiled vortex loops $\mathcal{T}_{1,q}$ with $q = 1 \sim 6$ and $\lambda = 0.1$, 0.3, 0.5 and 0.7 at (*a*) $t^* = 0$ and (*b*) $t^* = 10$. Each vortex is visualized by the isosurface of $|\boldsymbol{\omega}| = 0.04\omega_0$ colour-coded by the helicity density.

and the dissipation peak is higher for the loops with larger $q$, because their initial coils are closer to each other and more reconnections occur at the same time. This trend is projected that $\lambda_c$ and the vortex reconnection time decrease with the further increase of $q$.

Figure 15 compares initial vortex loops and central loops left after reconnection for $\mathcal{T}_{1,4}$ and $\mathcal{T}_{1,6}$ with $\lambda = 0.5$ and $\lambda = 0.7$. We find that the vortices with larger $\lambda(t^* = 0)$ in figure 15(*c*,*d*) than those in figure 15(*a*,*b*) are converted to more stable central secondary loops with smaller $\lambda(t^* = 0)$. This relation is quantified by the average torus aspect ratio in (4.1) of the central secondary loop for all the reconnection cases at time $t^* = 10$ in table 3.

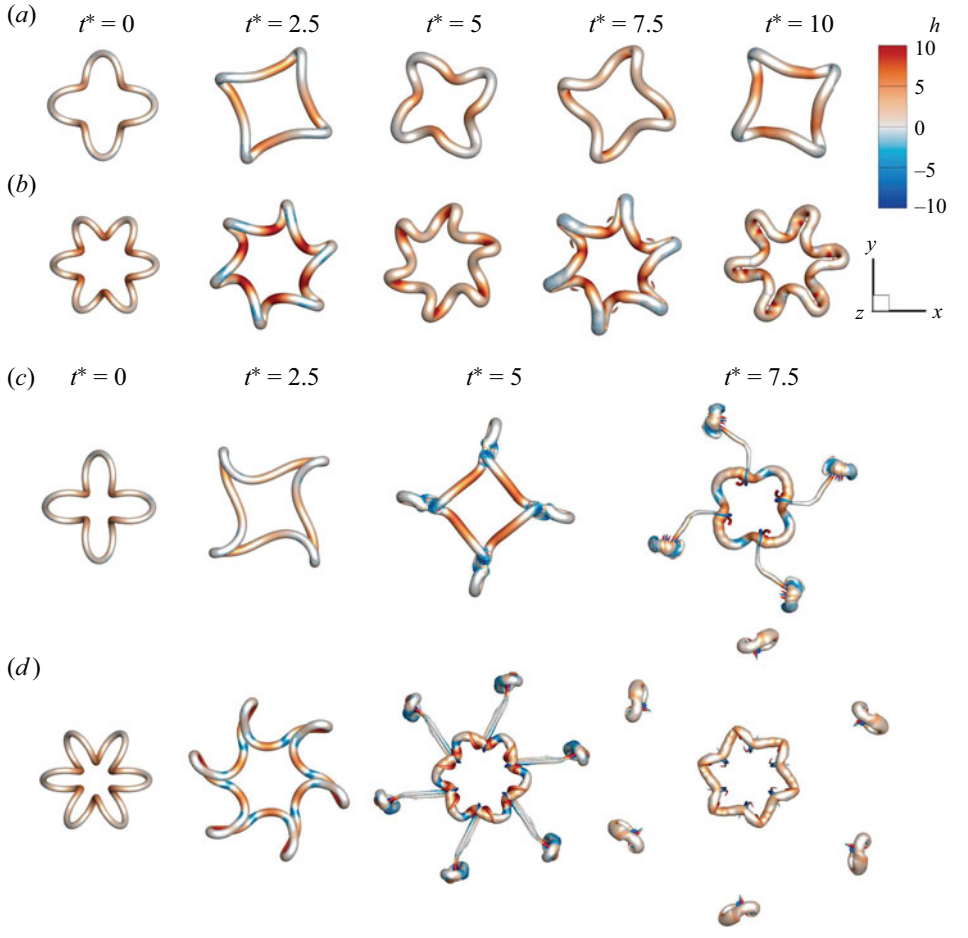


Figure 13. Evolution of the isosurface of $|\boldsymbol{\omega}| = 0.04\omega_0$ for vortices (*a*,*c*) $\mathcal{T}_{1,4}$ and (*b*,*d*) $\mathcal{T}_{1,6}$ with (*a*,*b*) $\lambda = 0.3$ and (*c*,*d*) $\lambda = 0.5$. The surfaces are colour-coded by the helicity density. For vortex $\mathcal{T}_{1,4}$ with $\lambda = 0.5$ at $t^* = 7.5$, the central loop has $|\boldsymbol{\omega}|_{max} = 68.92$ and $\Gamma = 1.02$, and the secondary loop has $|\boldsymbol{\omega}|_{max} = 81.71$ and $\Gamma = 1.09$. For vortex $\mathcal{T}_{1,6}$ with $\lambda = 0.5$ at $t^* = 7.5$, the central loop has $|\boldsymbol{\omega}|_{max} = 52.86$ and $\Gamma = 0.995$, and the secondary loop has $|\boldsymbol{\omega}|_{max} = 53.78$ and $\Gamma = 1.00$.

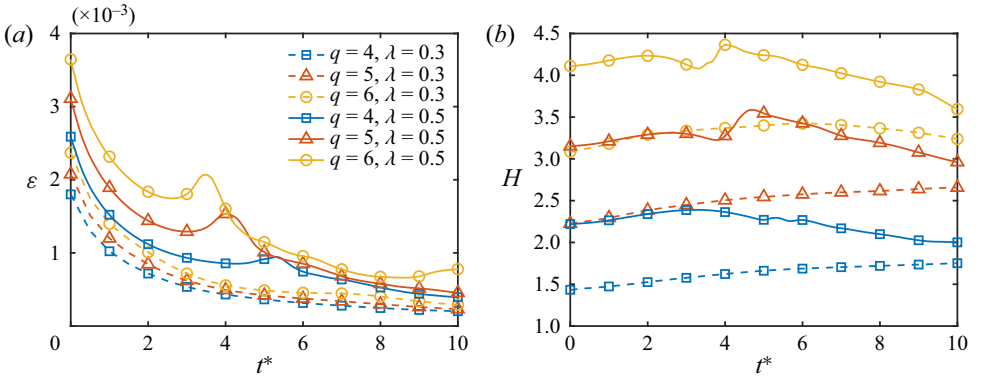


Figure 14. Evolution of (*a*) the mean dissipation rate and (*b*) total helicity for vortices $\mathcal{T}_{1,4}$, $\mathcal{T}_{1,5}$ and $\mathcal{T}_{1,6}$ with $\lambda = 0.5$ and 0.7.

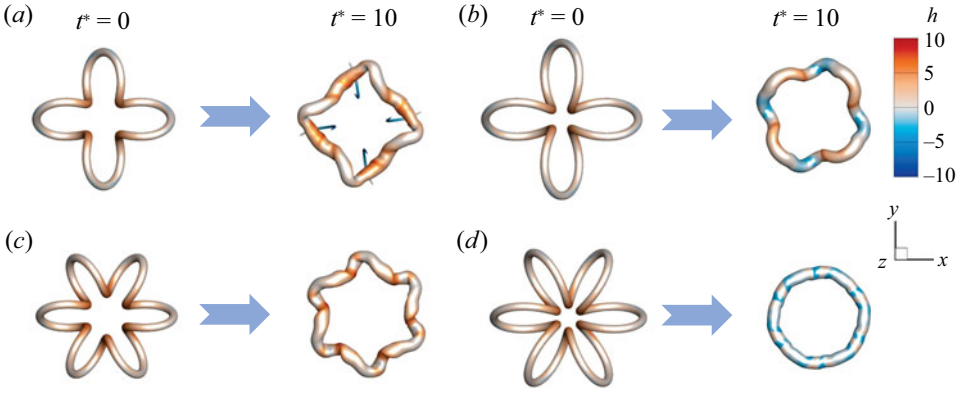


Figure 15. Geometric transformation of vortices (*a*,*b*) $\mathcal{T}_{1,4}$ and (*c*,*d*) $\mathcal{T}_{1,6}$ with (*a*,*c*) $\lambda = 0.5$ and (*b*,*d*) $\lambda = 0.7$ from the initial vortex loop to the central secondary loop via vortex reconnection. Each vortex is visualized by the isosurface of $|\boldsymbol{\omega}| = 0.04\omega_0$ colour-coded by the helicity density.

| Torus unknot type | $\mathcal{T}_{1,3}$ | $\mathcal{T}_{1,4}$ | $\mathcal{T}_{1,4}$ | $\mathcal{T}_{1,5}$ | $\mathcal{T}_{1,5}$ | $\mathcal{T}_{1,6}$ | $\mathcal{T}_{1,6}$ |
|---|---|---|---|---|---|---|---|
| Initial $\lambda$ | 0.7 | 0.5 | 0.7 | 0.5 | 0.7 | 0.5 | 0.7 |
| $\bar{\lambda}$ at $t^* = 10$ | 0.227 | 0.228 | 0.150 | 0.229 | 0.099 | 0.174 | 0.036 |

Table 3. Average torus aspect ratio for central vortex loops after the first vortex reconnection.

Since the thickness of vortex tubes grows with time due to viscous diffusion, a vortex loop must have local reconnection or self-intersection eventually. Before a finite time, e.g. $t^* = 10$ in figure 12(*b*), we observe a quasi-cycle of stretching and relaxation for small $\lambda$ and $q$ and clear reconnection events for large $\lambda$ and $q$. Based on this observation, we plot a stability diagram in figure 16 for the 24 vortex torus unknots with initial configurations shown in figure 12(*a*). The stable and unstable cases are marked by different symbols, and they are divided by a critical curve as an approximation of $\lambda_c$ in terms of $q$.

The transition route from the coiled vortex loop to the secondary loop via reconnection is marked by the arrows in figure 16, where the drop of $\lambda$ is according to the quantitative results in table 3. Again, we show the trend that a more unstable vortex loop can be reconnected into a more stable secondary loop, which appears to maintain the simple vortex topology and reduce the helicity variation of $\mathcal{T}_{1,q}$.

### 4.4. *Transition to turbulence for large winding numbers*

For large winding numbers $q$, the coiled loops in the unstable regime in figure 16 can have a transition to turbulence (or a turbulent-like state) after vortex reconnection. For example, the evolution of vortex $\mathcal{T}_{1,12}$ with $\lambda = 0.5$ and $q = 12$ in figure 17 differs from the bridging reconnections with $q = 4$ and 6 in figure 13(*c*,*d*). At the initial time, the coils are very close to each other, particularly on the inner side. The adjacent vortex tubes on the inner side are nearly parallel, and they undergo strong vortex interactions at $t^* = 2.5$ in the early stages. The tubular structure breaks up into a hierarchy of small-scale vortical structures at $t^* = 5$, triggering sudden transition to turbulence from the inner to outer sides. At $t^* = 10$, the thread-like vortex tubes are intertwined with each other, similar to the tangle of vortex tubes identified in turbulence (Xiong & Yang 2019*b*).

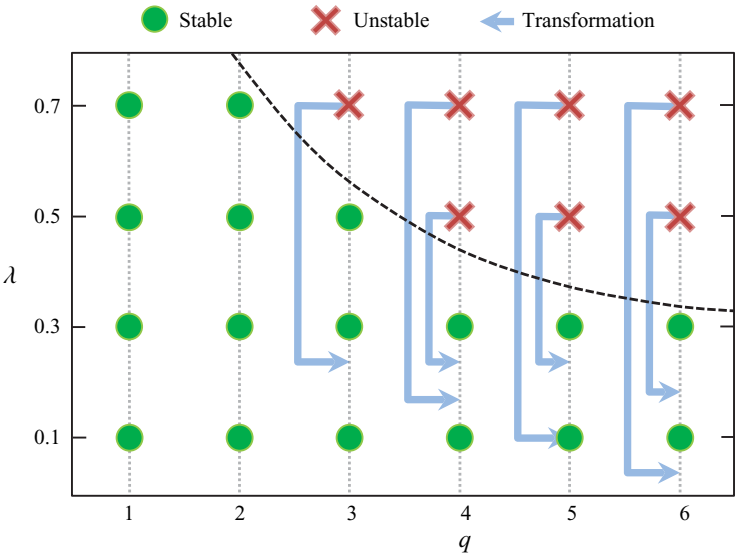


Figure 16. Stability diagram of coiled vortex loops, corresponding to the visualization in figure 12. The dashed line denotes the critical curve to demarcate stable and unstable regimes, and the arrows denote the geometric transformation illustrated in figure 15 via the vortex reconnection.

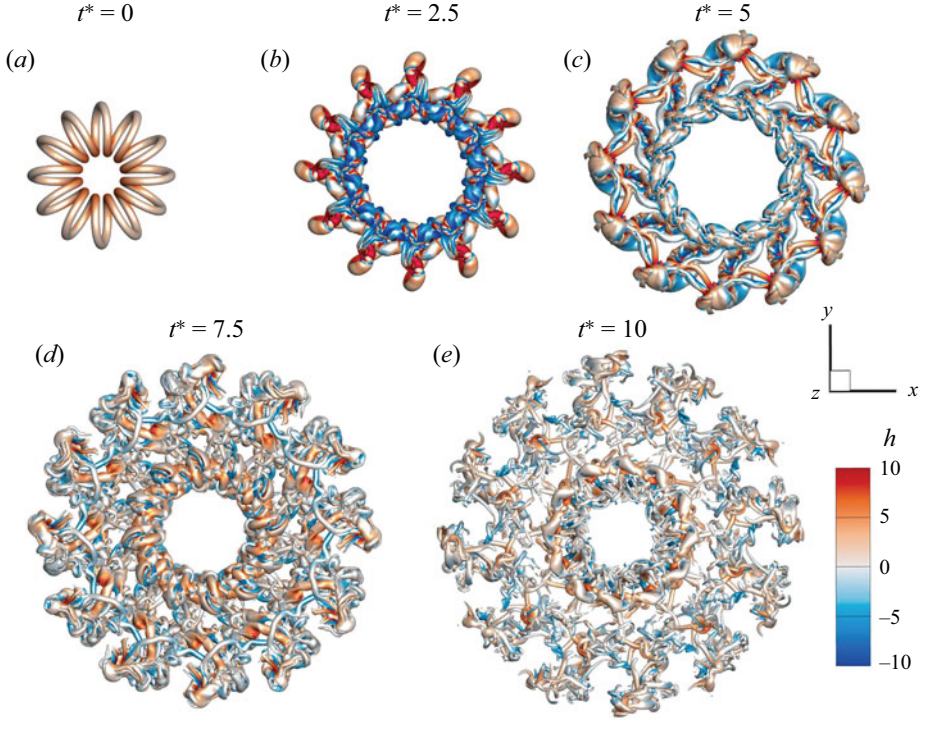


Figure 17. Evolution of the isosurface of $|\boldsymbol{\omega}| = 0.04\omega_0$ for vortex $\mathcal{T}_{1,12}$ with $\lambda = 0.5$. Surfaces are colour-coded by the helicity density.

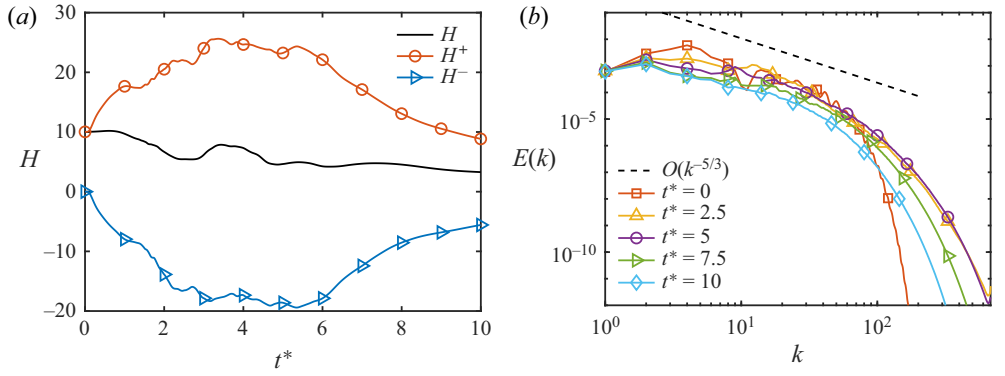


Figure 18. Evolution of (*a*) the total helicity with the positive–negative decomposition and (*b*) the energy spectrum of vortex $\mathcal{T}_{1,12}$ with $\lambda = 0.5$.

The time evolution of $H$, $H^+$ and $H^-$ of this vortex $\mathcal{T}_{1,12}$ in figure 18(*a*) shows that the total helicity generally decays in the early stage, and then undergoes a notable jump during the transition at $t^* = 2.5 \sim 5$. Both $|H^+|$ and $|H^-|$ surge before the transition due to the emergence of oppositely polarized helicity structures (Yao *et al.* 2021), and then decay after the transition due to viscous dissipation as in decaying turbulence. The time evolution of the energy spectrum in figure 18(*b*) shows the migration of $E(k)$ from low wavenumbers $k \leq 50$ to high wavenumbers $k \geq 100$ during the transition, and a part of $E(k)$ is close to the $-5/3$ scaling at late times. The evolution of $E(k)$ is consistent with the flow visualization in figure 17, where large-scale tubular structures gradually break up into small-scale ones.

This case demonstrates that even a single vortex loop with the trivial topology can undergo transition to turbulence and indicates that the geometry is more important than the topology for vortex evolution in viscous flows. Additionally in the stability diagram in figure 16, there is a sub-region for the transition in the unstable regime at large $q$, which is different from the simple reconnection sub-region at small $q$.

## 5. Evolution of vortex torus knots and links $\mathcal{T}_{2,q}$

### 5.1. *Vortex merging for small torus aspect ratios*

The vortex $\mathcal{T}_{p,q}$ with $p \geqslant 2$ has the initial configuration of a knot or link, and it can undergo more complex topological transitions and helicity conversion than $\mathcal{T}_{1,q}$. In this section we focus on $\mathcal{T}_{2,q}$ with various torus aspect ratios.

We start from vortex $\mathcal{T}_{2,q}$ with small $\lambda = 0.1$. The initial configuration of $\mathcal{T}_{2,q}$ with $q = 1 \sim 6$ and $\lambda = 0.1$ is visualized in figure 19, where $\mathcal{T}_{2,1}$ is topologically trivial, $\mathcal{T}_{2,3}$ and $\mathcal{T}_{2,5}$ are trefoil and cinquefoil knots, respectively, and $\mathcal{T}_{2,2}$, $\mathcal{T}_{2,4}$ and $\mathcal{T}_{2,6}$ are links containing two components. Table 4 lists the initial total writhing number $W_r = \sum_i W_{r,i}$ and linking number $L_k = \sum_{i \neq j} L_{k,ij}$ calculated by (2.3) and (2.7), respectively. From the helicity density distribution in figure 19 and the helicity components in table 4, the total helicity $H = W_r + L_k$ increases with $q$.

For small $\lambda$, the cross-section of $\mathcal{T}_{p,q}$ has a pair of vortices which are close to each other and have nearly the same vortex-axis direction. This type of vortex pairs can merge together in viscous flows when the ratio of the Lamb–Oseen core size $a$ to the distance $b$ of vortex cores satisfies $a/b > 0.22$ (Le Dizes & Verga 2002). The initial configuration of

| Torus knot/link | $\mathcal{T}_{2,1}$ | $\mathcal{T}_{2,2}$ | $\mathcal{T}_{2,3}$ | $\mathcal{T}_{2,4}$ | $\mathcal{T}_{2,5}$ | $\mathcal{T}_{2,6}$ |
|---|---|---|---|---|---|---|
| $W_r$ | 0.996 | $1.5 \times 10^{-4}$ | 3.019 | 0.060 | 5.127 | 0.230 |
| $L_k$ | 0 | 2 | 0 | 4 | 0 | 6 |
| $W_r + L_k$ | 0.996 | 2.000 | 3.019 | 4.060 | 5.127 | 6.230 |

Table 4. Initial writhing and linking numbers of vortex $\mathcal{T}_{2,q}$ in figure 19.

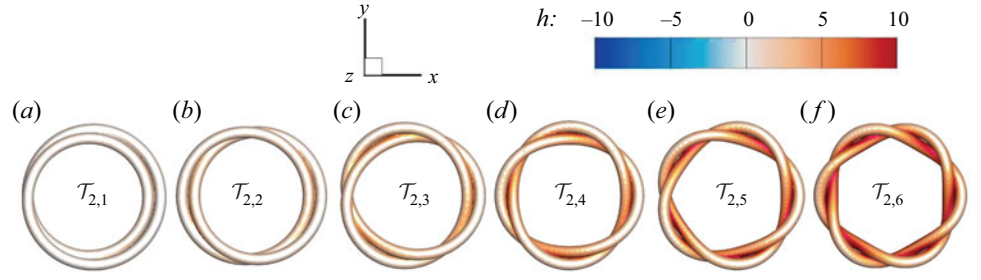


Figure 19. Initial configurations of vortex $\mathcal{T}_{2,q}$ with $q = 1 \sim 6$ and $\lambda = 0.1$. Each vortex is visualized by the isosurface of $|\boldsymbol{\omega}| = 0.04\omega_0$ colour-coded by the helicity density.

$\mathcal{T}_{2,q}$ with $\lambda = 0.1$ has a pair of adjacent vortex tubes, satisfying the merging criterion as

$$\frac{a}{b} = \frac{\sqrt{2}\sigma_0}{2\lambda R_t} = \frac{1}{16\sqrt{2\pi}\lambda} = 0.249 > 0.22, \tag{5.1}$$

where the estimation of $a$ is consistent with the method in Le Dizes & Verga (2002), so the adjacent vortex tubes merge in the early stage of evolution. This criterion also suggests that the vortex merging for $\mathcal{T}_{2,q}$ occurs for $\lambda < 0.113$.

Taking $\mathcal{T}_{2,3}$ for example, the time evolution of the trefoil vortex in figure 20 shows the merging of adjacent vortex tubes at very early times. The knotted tube rapidly merges into a vortex ring. Figure 21 plots the contour of $|\boldsymbol{\omega}|$ on the $y$–$z$ slice at $x = \pi$. A pair of isolated and co-directional vortices at $t^* = 0$ merge at $t^* = 0.5$. This merging produces spiral structures on the periphery of the merged vortex core with the emergence of large opposite $h$, similar to the reconnections in figure 13 and in Yao *et al.* (2021). The vortex merging is almost complete and the spiral arms are dissipated at $t^* = 2.5$, leaving a simple vortex ring with doubled circulation $\Gamma_m = 2\Gamma_0$. Then, the vortex lines continue to be coiled on the vortex ring after the merging in figure 20.

The rapid topological transition causes very fast helicity conversion. Figure 22 plots the helicity topological decomposition of vortex $\mathcal{T}_{2,3}$ with $\lambda = 0.1$ at very early times $t^* \leq 0.5$ and during the entire evolution. At $t^* \approx 0.35$, the circulation of the vortex doubles, and the falling $\Gamma^2 W_r$ and surging $\Gamma^2 \tilde{T}_w$ imply that the writhe helicity is fully converted into the generalized twist helicity. In the final stage of the merging, the interaction of the spiral vortices causes $H$ to increase via the growth of $\tilde{T}_w$. The total helicity of the initial vortex $\mathcal{T}_{2,q}$ is $H = \Gamma^2(W_r + L_k)$ with zero twist, while it becomes $H = \Gamma^2 \tilde{T}_w$ dominated by the twist after the vortex merging. This complete helicity conversion from $W_r$ to $T_w$ is much faster than that due to the stretching and compression of coiled vortex loops (see Scheeler *et al.* 2017).

At late times, the twisted vortex lines gradually become parallel to the vortex core line under the viscous effect (see figure 20), which manifests in the decay of $T_w$

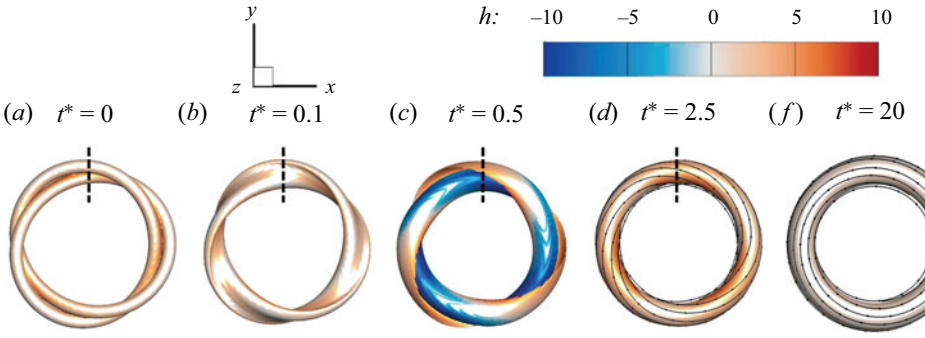


Figure 20. Evolution of the isosurface of $|\boldsymbol{\omega}| = 0.04\omega_0$ for vortex $\mathcal{T}_{2,3}$ with $\lambda = 0.1$ at $t^* = 0$, 0.1, 0.5, 2.5 and 20 (from *a–e*). Surfaces are colour-coded by the helicity density. Some typical vortex lines are plotted at $t^* = 2.5$ and 20.

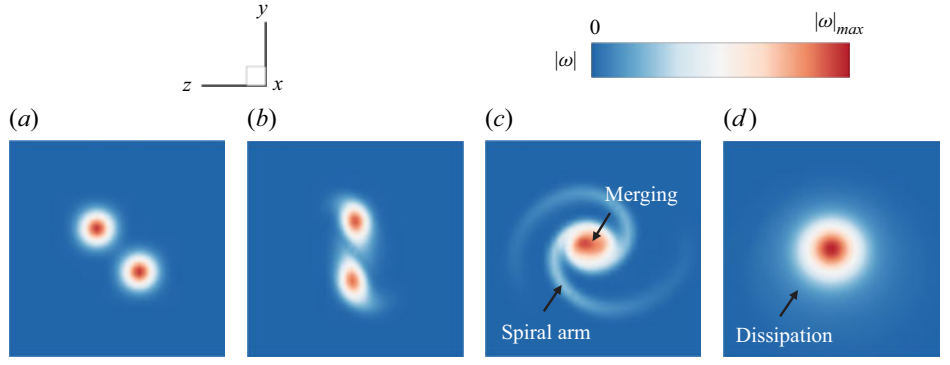


Figure 21. Evolution of $|\boldsymbol{\omega}|$ on the $y$–$z$ slice (marked by the dashed line in figure 20) for vortex $\mathcal{T}_{2,3}$ with $\lambda = 0.1$ at (*a*) $t^* = 0$, (*b*) $t^* = 0.1$, (*c*) $t^* = 0.5$ and (*d*) $t^* = 2.5$.

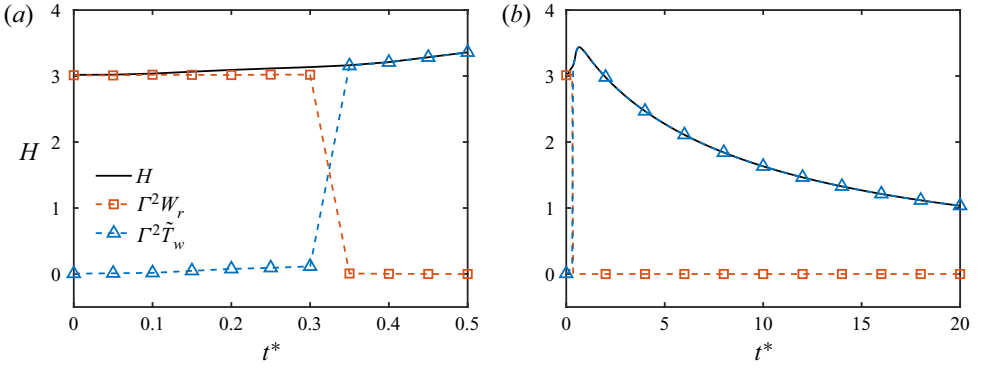


Figure 22. Evolution of the helicity and its topological decomposition of vortex $\mathcal{T}_{2,3}$ with $\lambda = 0.1$ (*a*) in the early stage $t^* \leq 0.5$ and (*b*) during the entire evolution.

(Scheeler *et al.* 2017; Xiong & Yang 2020). Figure 23(*a*) plots the time evolution of $H$, $H^+$ and $H^-$ of vortex $\mathcal{T}_{2,3}$ with $\lambda = 0.1$. All the helicity magnitudes surge during the incipient vortex merging, then quickly peak and slowly decay. The decay of $|H^-|$ is faster than $|H^+|$ so vortex lines gradually form a right-handed twisting structure. After the merging

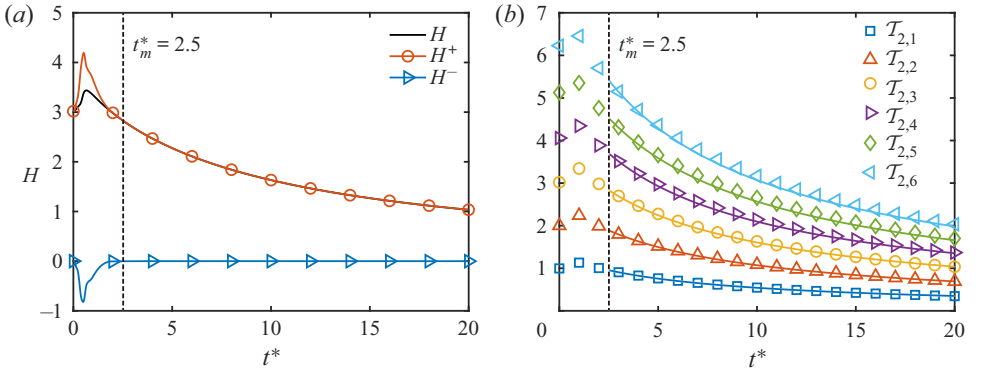


Figure 23. (*a*) Evolution of $H$, $H^+$ and $H^-$ of vortex $\mathcal{T}_{2,3}$ with $\lambda = 0.1$. (*b*) Comparison of the DNS results (symbols) and model estimations (solid lines) from (E10) for vortex $\mathcal{T}_{2,q}$ with $q = 1 \sim 6$ and $\lambda = 0.1$. The results of each case are represented in the same colour.

is complete around $t_m^* = 2.5$, $H^+$ and $H^-$ relax to $H$ and zero, respectively; $H$ for $\mathcal{T}_{2,q}$ with different $q$ decays with time in a self-similar way, i.e. the curves of $H(t^*)/H(t_m^*)$ for various vortex knots/links against $t^*$ collapse (not shown). In figure 23(*b*) this decay law is well estimated by the model (E10) developed in Appendix E.

### 5.2. *Topological degeneration for large torus aspect ratios*

For relatively large torus aspect ratios, previous studies reported that the torus (Xiong & Yang 2019*a*; Yao *et al.* 2021) or non-torus (Kida & Takaoka 1987; Kleckner & Irvine 2013; Zhao *et al.* 2021) trefoil vortex knot with $\lambda = 0.5$ is untied into coiled vortex loops during the bridging reconnection. This unknotting process implies a possible route for the topological degeneration of vortex knots/links, i.e. the decrease of the topological complexity (Kleckner *et al.* 2016; Liu *et al.* 2020) or values of $p$ and $q$ of the vortex core line in the evolution of $\mathcal{T}_{p,q}$.

We illustrate the topological degeneration of vortex $\mathcal{T}_{2,q}$ with $q = 1 \sim 6$ and $\lambda = 0.5$ through vortex reconnection in figure 24. The vortex knots or links are untied into two coiled vortex loops $\mathcal{T}_{1,q}$ via the primary reconnection. Then, the upper vortex loop has a smaller $\lambda$ than that of the lower one, so it is more stable in the further evolution as implied by the stability diagram in figure 16.

The lower loop $\mathcal{T}_{1,q}$ with large $q$, as discussed in § 4, can reconnect again and split into $q$ small vortex loops. In figure 24 the lower loop of $\mathcal{T}_{2,4}$ after unknotting has the secondary reconnection at $t^* = 20$. At the same time, the secondary reconnection of $\mathcal{T}_{2,5}$ and $\mathcal{T}_{2,6}$ have been completed, and the lower vortex loops break up into small-scale, turbulent-like structures which are then gradually dissipated. We remark that the vortex breakup is also related to the vortex tube radius at very large $Re$, as suggested in Appendix B. The lower loops tend to be more stable for thinner vortex tubes.

The vortex reconnection event coincides with the occurrence of the large helicity fluctuation and the peak of the dissipation rate (see Xiong & Yang 2019*a*). Figure 25 shows the time evolution of $H$ and $\varepsilon$ of vortex $\mathcal{T}_{2,q}$ with $q = 1 \sim 6$ and $\lambda = 0.5$. For $\mathcal{T}_{2,1}$, $\mathcal{T}_{2,2}$ and $\mathcal{T}_{2,3}$ with single reconnection during the evolution, $H$ is almost conserved except for the fluctuation at the reconnection time. By contrast, $H$ of $\mathcal{T}_{2,5}$ and $\mathcal{T}_{2,6}$ decays shortly after the first reconnection due to vortex breakup, and the decay rate is mitigated when $H$ is low at late times. This indicates that the helicity stored in the lower loops is reduced in the vortex

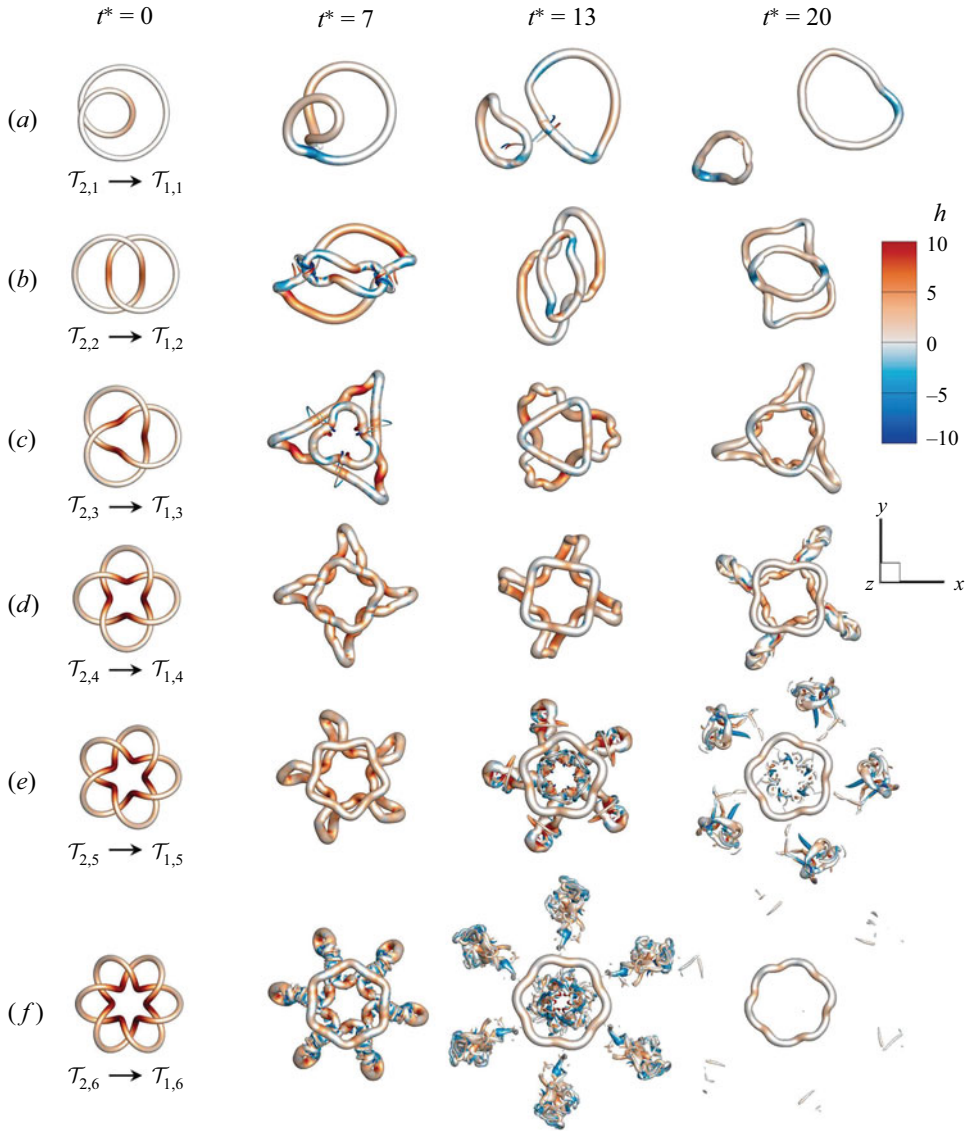


Figure 24. Evolution of the isosurface of $|\boldsymbol{\omega}| = 0.04\omega_0$ for vortex $\mathcal{T}_{2,q}$ with $q = 1 \sim 6$ and $\lambda = 0.5$ at $t^* = 0$, 7, 13 and 20. Surfaces are colour-coded by the helicity density.

breakup, while the helicity for the stable upper loop is conserved. The number and time of peaks of $\varepsilon$ indicate that the evolution of $\mathcal{T}_{2,5}$ or $\mathcal{T}_{2,6}$ has two significant reconnections, and the first reconnection time of $\mathcal{T}_{2,q}$ decreases with the increase of $q$.

### 5.3. *Transition to turbulence for moderate torus aspect ratios*

Distinct from the vortex merging for small $\lambda$ and the topological degeneration for large $\lambda$, vortex $\mathcal{T}_{2,q}$ with moderate $\lambda$ can directly break up into turbulence via the first vortex reconnection. Figure 26 plots the time evolution of vortex $\mathcal{T}_{2,3}$ with $\lambda = 0.3$. In the early stage, the vortex tubes approach each other and begin to reconnect, similar to the cases

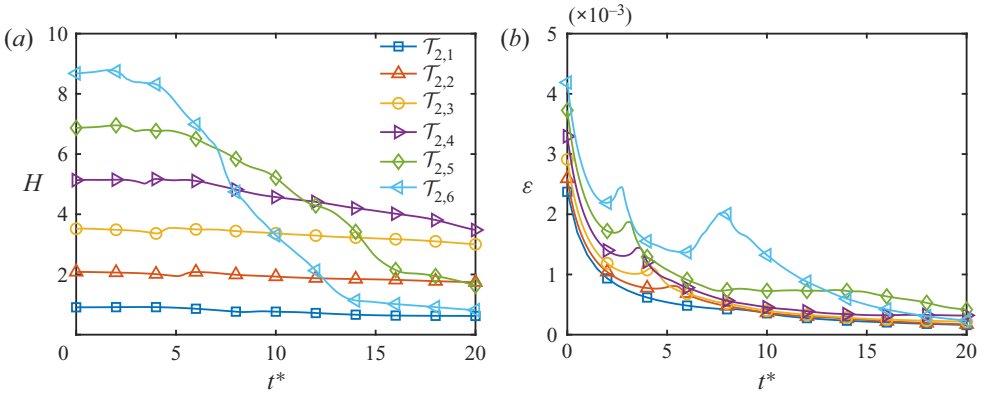


Figure 25. Evolution of (*a*) the total helicity and (*b*) dissipation rate of vortex $\mathcal{T}_{2,q}$ with $q = 1 \sim 6$ and $\lambda = 0.5$.

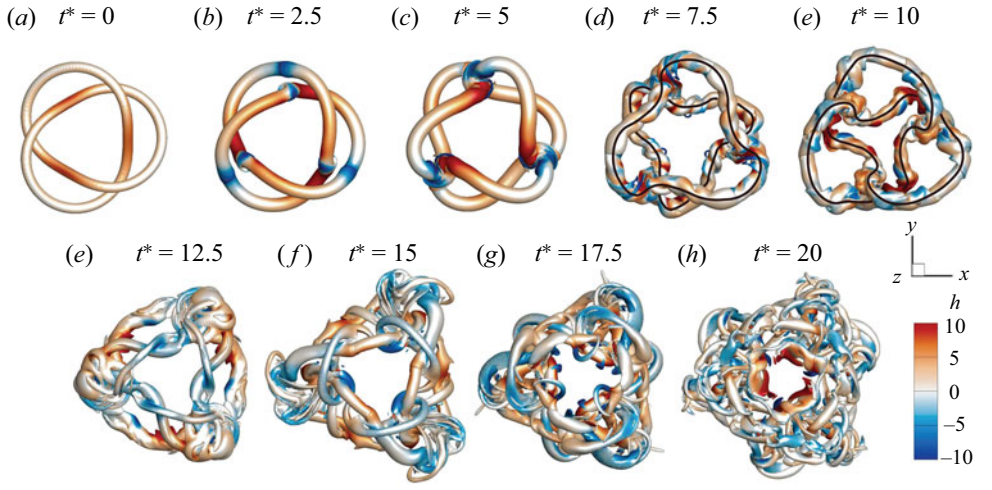


Figure 26. Evolution of the isosurface of $|\boldsymbol{\omega}| = 0.04\omega_0$ for vortex $\mathcal{T}_{2,3}$ with $\lambda = 0.3$ at $t^* = 0$, 2.5, 5, 7.5, 10, 12.5, 15, 17.5 and 20. Surfaces are colour-coded by the helicity density. Black solid lines at $t^* = 7.5$ and 10 sketch the topology of vortex core lines.

for large $\lambda$. Then, the vortex knot tends to separate into two loops with similar shapes at $t^* = 7.5$.

The subsequent evolution and interaction of the two coaxial vortex loops depend on their $z$-direction forward velocity. Recall that the forward velocity of an isolated vortex ring with the constant circulation and thickness is inversely proportional to $R_t$. In addition, the forward velocity also decreases with the average torus aspect ratio $\bar{\lambda}$ for the same average radius $\bar{R}$ in figure 9(*c*). For vortex $\mathcal{T}_{2,q}$ with large $\lambda$ (see figure 24*a–c*), $\bar{\lambda}$ and $\bar{R}$ of the upper loop are much smaller than those of the lower loop. This geometric difference causes a large difference in the forward velocity between the upper and lower loops, i.e. the separation of the two loops after reconnection.

In contrast, the two vortex loops with similar $\bar{\lambda}$ and $\bar{R}$ after the first reconnection of $\mathcal{T}_{p,q}$ at $t^* = 5$ have comparable forward velocities, so they cannot be fully separated after reconnection. During the incomplete separation, they can even reversely evolve into the

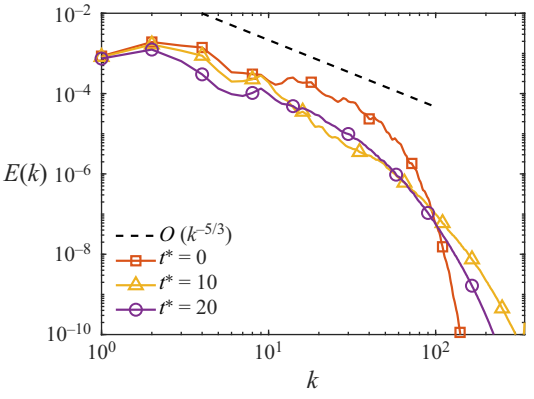


Figure 27. Energy spectra of vortex $\mathcal{T}_{2,3}$ with $\lambda = 0.3$ at $t^* = 0$, 10 and 20.

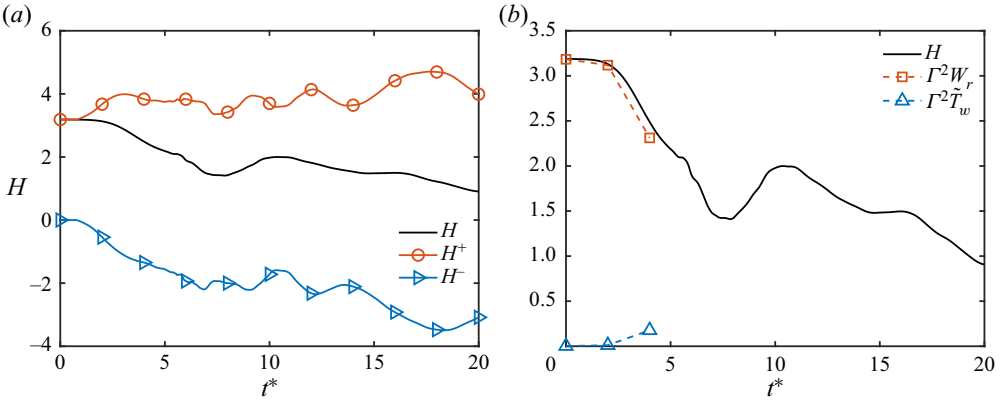


Figure 28. Evolution of the helicity with the (*a*) positive–negative and (*b*) topological decompositions for vortex $\mathcal{T}_{2,3}$ with $\lambda = 0.3$.

former trefoil structure at $t^* = 10$ in figure 26. The large-scale oscillating motion causes the strong interaction of coaxial upper and lower loops to trigger vortex breakup and transition to turbulence. In figure 27 the energy spectrum is broadened at high wavenumber region $k \geq 100$ in the time evolution, consistent with the generation of small-scale vortical structures in figure 26, and decays at small and moderate $k$. At $t^* = 20$, the scaling of $E(k)$ is close to $-5/3$.

Figure 28(*a*) plots the time evolution of positive, negative and total helicities. In general, $H$ decays, and $|H^+|$ and $|H^-|$ grow with time. For comparison, $|H^-|$ decays to zero in the vortex merging case in figure 23(*a*). The statistically symmetric growths of $|H^+|$ and $|H^-|$ are consistent with the emergence of small-scale vortical structures, as statistically even generations of $h^+$ and $h^-$ in isotropic turbulence.

Figure 28(*b*) shows the evolution of helicity components in (4.4). Before the reconnection, $W_r$ drops and $\tilde{T}_w$ rises as in the coiled loop in figure 11 and the trefoil vortex knot in figures 10 and 16 in Yao *et al.* (2021). Subsequently, the incomplete reconnection and the transition to turbulence pose a great challenge to identify the vortex core line, so that the topological decomposition of helicity in (4.4) becomes invalid after $t^* = 5$.

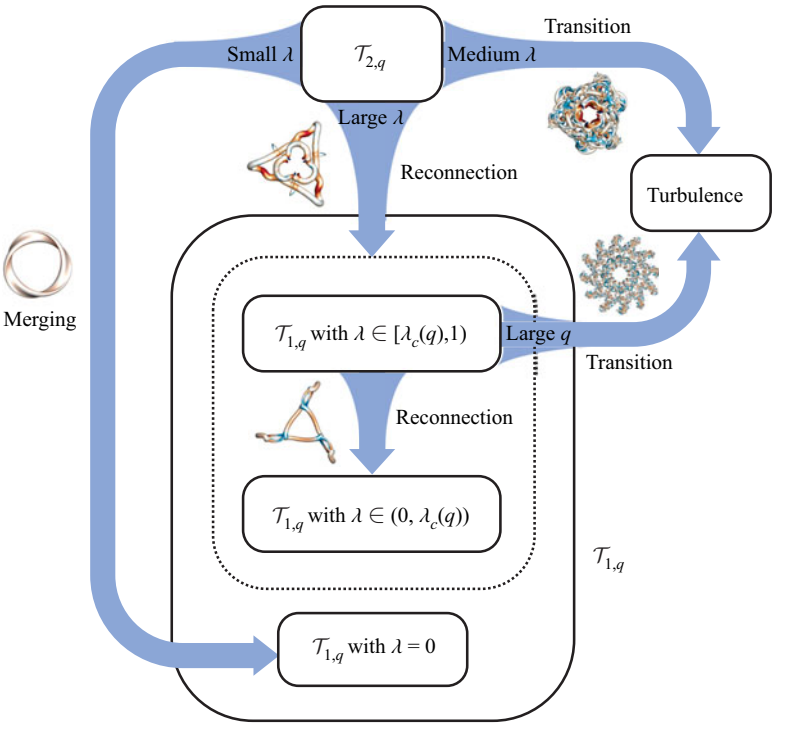


Figure 29. Evolutionary route map of vortex $\mathcal{T}_{2,q}$.

It can be expected that twisting and winding of vortex lines are further intensified in the transition, which needs a new method to characterize in future work.

### 5.4. *Route map of topological transitions*

Vortex knots and links can serve as simplified model vortices for complex flows. We demonstrate that the evolution of even the simple vortex $\mathcal{T}_{2,q}$ with different torus aspect ratios has three independent topological transition routes: merging, reconnection and transition to turbulence. The evolutionary route map of $\mathcal{T}_{2,q}$ is sketched in figure 29.

(i) For small $\lambda$, vortex merging occurs at very early times. This rapid process transforms a knot or link, as $\mathcal{T}_{2,q}$ with $\lambda \to 0$, into a vortex ring, and converts all the initial writhe and link helicities into the generalized twist helicity.

(ii) For large $\lambda$, the vortex knot or link is untied into upper and lower coiled loops $\mathcal{T}_{1,q}$ during the primary vortex reconnection, along with a partial conversion of the writhe and link helicities to generalized twist helicity. Then, the upper one with small $\lambda$ tends to be stable, while the lower one with large $\lambda \in [\lambda_c(q), 1)$ in the unstable regime in figure 16 has the secondary reconnection to split into more stable vortex loops with $\lambda \in (0, \lambda_c(q), 1)$. In addition, the lower loop with a very large $q$ can have transition to a turbulent-like state.

(iii) For moderate $\lambda$, the vortex reconnection is incomplete. The two interconnected vortex loops with similar geometries have strong interaction to trigger the transition to turbulence and make the topological decomposition of $H$ invalid.

## 6. Conclusions

We study the evolution of vortex torus knots and links in viscous flows. In particular, we focus on the transition between different topological states and the conversion between writhe and generalized twist helicity components of the knots and links during the vortex interaction. A series of DNS cases are carried out for vortices $\mathcal{T}_{p,q}$ of different topologies and geometries with $p = 1, 2$, $q = 1 \sim 12$ and $\lambda = 0.1 \sim 0.7$. The initial knots and links have $T_w = 0$.

For coiled vortex loops $\mathcal{T}_{1,q}$, the torus aspect ratio $\lambda$ and the winding number $q$ impact the evolutionary topology and geometry. For small $\lambda$, $\mathcal{T}_{1,q}$ shows a quasi-periodic stretching-relaxation evolution with nearly conserved $W_r$ and vanishing $\tilde{T}_w$, so the total helicity is generally conserved. As $\lambda$ is larger than a critical value $\lambda_c(q)$ that decreases with $q$, the loop reconnects under self-induction and breaks up into a central coiled loop with smaller $\lambda$ surrounded by $q$ small secondary loops. The vortex reconnection leads to helicity conversion from $W_r$ to $\tilde{T}_w$ and the transient growth of $H$. This is consistent with the result in Yao *et al.* (2021) and Zhao & Scalo (2021) for trefoil vortex knots, indicating the similarity of the helicity dynamics in the reconnection of knotted vortex tubes. For very large $q$, the initially adjacent coils can undergo strong interactions to trigger sudden transition to turbulence. The stability diagram of vortex $\mathcal{T}_{1,q}$ in terms of $q$ and $\lambda$ is presented in figure 16.

For vortex torus knots and links with $p = 2$, there are three topological transition routes of the vortex evolution: merging, reconnection and transition to turbulence. The topological transition depends not only on the initial topology but also on the initial geometry of $\mathcal{T}_{2,q}$. For small $\lambda$, vortex $\mathcal{T}_{2,q}$ rapidly merges into a vortex ring with complete helicity conversion from writhe and link to twist. For large $\lambda$, the vortex knot or link is untied into upper and lower coiled loops via the first reconnection, with a partial conversion from writhe and link to twist. Then, the lower loop with large $\lambda$ in the unstable regime in figure 16 can undergo secondary reconnection to split into $q$ small loops, and this loop with very large $q$ can break up into turbulence. For moderate $\lambda$, the incomplete reconnection of tangled vortex loops with strong vortex interactions triggers transition to turbulence, and the topological decomposition of $H$ becomes invalid. The evolutionary route map of $\mathcal{T}_{2,q}$ is presented in figure 29.

The present study can be extended to more complex vortex knots and links with $p \geq 3$ having much more complex pathways of the topological transition and conversion mechanisms of helicity components. The topological evolution and helicity dynamics of vortex knots and links can shed light on the evolution of tangled vortex tubes in turbulence, but whether the turbulence can be modelled by an ensemble of vortex knots and links is an open problem.

**Funding.** Numerical simulations and visualization were carried out on the Tianhe-2A supercomputer in Guangzhou, China. This work has been supported in part by the National Natural Science Foundation of China (grant nos 11925201, 91952108, 11988102 and 91841302), the National Key R&D Program of China (No. 2020YFE0204200) and the Xplore Prize.

**Declaration of interests.** The authors report no conflict of interest.

**Author ORCIDs.**
Weiyu Shen https://orcid.org/0000-0003-4385-8835;
Jie Yao https://orcid.org/0000-0001-6069-6570;
Fazle Hussain https://orcid.org/0000-0002-2209-9270;
Yue Yang https://orcid.org/0000-0001-9969-7431.

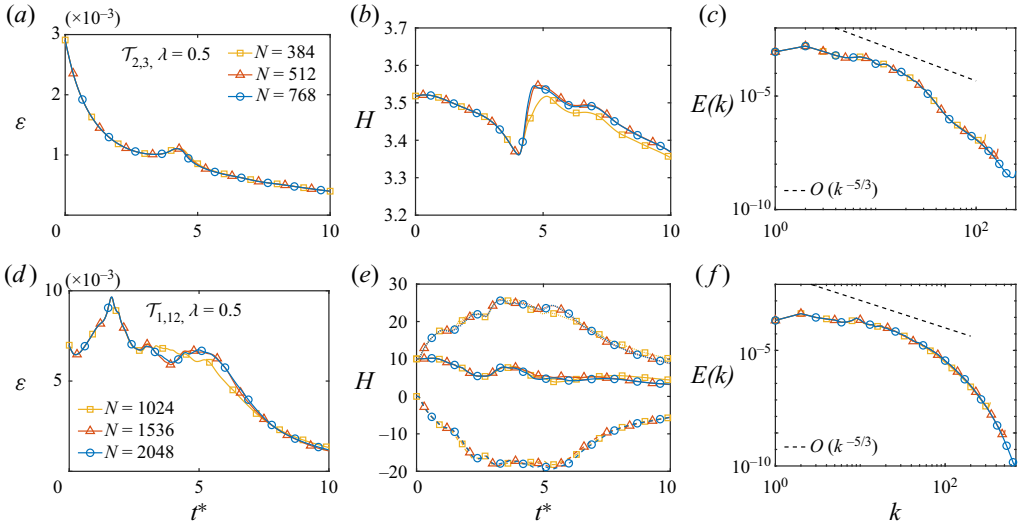


Figure 30. Grid convergence tests of the mean dissipation rate, total helicity and energy spectrum for (*a–c*) vortex $\mathcal{T}_{2,3}$ and (*d–f*) vortex $\mathcal{T}_{1,12}$ with $\lambda = 0.5$ and $Re = 2000$. The dotted and dashed lines in (*e*) denote $H^+$ and $H^-$, respectively. The energy spectra are at $t^* = 4.2$ in (*c*) and $t^* = 5$ in (*f*) when the mean dissipation rate reaches the last peak.

## Appendix A. Grid convergence test

The grid convergence test for the mean dissipation rate, total helicity, energy spectrum and helicity budget is presented for two representative cases with $Re = 2000$. First, the case of the trefoil vortex knot $\mathcal{T}_{2,3}$ with $\lambda = 0.5$ has the typical bridging reconnection. Figure 30(*a*,*b*) plots the time evolution of the mean dissipation rate and the total helicity with different grid resolutions of $N^3 = 384^3$, $512^3$ and $768^3$, and both the quantities converge for $N^3 = 768^3$ in the entire evolution. Figure 30(*c*) shows that all energy spectra with different resolutions at the reconnection time converge.

Second, vortex $\mathcal{T}_{1,12}$ with $\lambda = 0.5$ has the most intensive vortex interaction in the present study. Due to the strong local velocity gradient in the transition, three finer meshes with $N^3 = 1024^3$, $1536^3$ and $2048^3$ are used. In figure 30(*d*) the time evolution of the mean dissipation rate is well converged from $N^3 = 1024^3$ to $2048^3$. In figure 30(*e*) the time evolution of the total helicity with the positive–negative decomposition also fairly converges for $2048^3$. Although the total helicities for $N^3 = 1536^3$ and $2048^3$ are slightly different around $t^* = 5$, the evolutions of $H^+$ or $H^-$ for both grids are almost identical. In figure 30(*f*) the energy spectra for the three grids at $t^* = 5$ also collapse.

Moreover, the helicity budget

$$\frac{\mathrm{d}H}{\mathrm{d}t} = -2\nu \iiint \boldsymbol{\omega} \cdot (\boldsymbol{\nabla} \times \boldsymbol{\omega}) \, \mathrm{d}\mathcal{V} \tag{A1}$$

is checked to be close, further validating the simulation accuracy (Zhao *et al.* 2021), where $\boldsymbol{\omega} \cdot (\boldsymbol{\nabla} \times \boldsymbol{\omega})$ is the super-helicity density (Brissaud *et al.* 1973; Hide 1989). We compare the helicity production term on the right-hand side of (A1) obtained by integrating the super-helicity density and $\mathrm{d}H/\mathrm{d}t$ on the left-hand side of (A1) obtained by differentiating the time series of $H(t)$. Figure 31 shows excellent agreement of the two terms for vortex $\mathcal{T}_{2,3}$ on $N^3 = 512^3$ and $\mathcal{T}_{1,12}$ on $N^3 = 2048^3$.

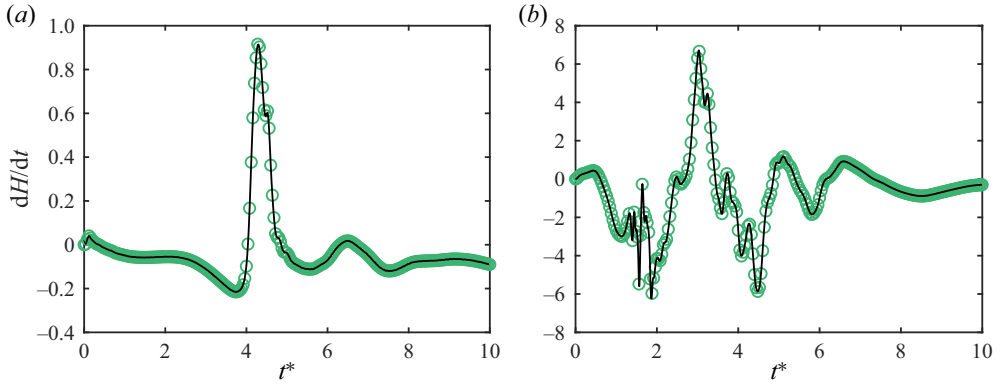


Figure 31. Helicity budget of (*a*) vortex $\mathcal{T}_{2,3}$ with $\lambda = 0.5$ on $N^3 = 512^3$ and (*b*) $\mathcal{T}_{1,12}$ with $\lambda = 0.5$ on $N^3 = 2048^3$. The circles denote the helicity production term on the right-hand side of (A1) obtained by integrating the super-helicity density, and the solid lines denote $\mathrm{d}H/\mathrm{d}t$ in (A1) obtained by differentiating the time series of $H(t)$.

## Appendix B. Effects of the vortex tube thickness

For a coiled vortex loop, the tube thickness $\sigma$ affects its self-induced velocity and, hence, its evolution. In addition, $\sigma$ also plays an important role in the reconnection process, i.e. the reconnection time and rate. Therefore, we examine the effect of the vortex tube thickness on the topological transition of the coiled vortex loop, in particular, on the critical torus aspect ratio $\lambda_c$.

Due to the spatial requirement for resolving the vortex core and small scales generated during reconnection, it is rather challenging to employ DNS for studying the evolution of coiled vortex loops with very small $\sigma$. Hence, instead, we employ the vortex filament method (VFM) – a widely used and powerful tool for studying the interaction of vortex filaments and quantized vortices (Ricca *et al.* 1999; Hänninen & Baggaley 2014; Kimura & Moffatt 2017).

Within the VFM, the velocity at a point $\boldsymbol{r}$ induced by a vortex filament $\boldsymbol{s}$ with circulation $\Gamma$ is given by the BS law (Schwarz 1985)

$$\boldsymbol{u}_s(\boldsymbol{r}, t) = \frac{\Gamma}{4\pi} \int \frac{(\boldsymbol{s}_1 - \boldsymbol{r}) \times \mathrm{d}\boldsymbol{s}_1}{|\boldsymbol{s}_1 - \boldsymbol{r}|^3}, \tag{B1}$$

where $\boldsymbol{s}_1$ refers to a particular point on $\boldsymbol{s}$. The integral (B1) becomes singular when evaluating the velocity at a particular point on the vortex. This issue can be resolved by considering the finite vortex tube thickness and very large $Re$ (Schwarz 1985; Hänninen & Baggaley 2014), and then (B1) becomes

$$\boldsymbol{u}_s(\boldsymbol{s}, t) = \frac{\Gamma}{4\pi} \boldsymbol{s}' \times \boldsymbol{s}'' \ln\left(\frac{2\sqrt{l_+ l_-}}{\mathrm{e}^{1/2} r_v}\right) + \frac{\Gamma}{4\pi} \int_{\boldsymbol{s}_1 \neq \boldsymbol{s}} \frac{(\boldsymbol{s}_1 - \boldsymbol{s}) \times \mathrm{d}\boldsymbol{s}_1}{|\boldsymbol{s}_1 - \boldsymbol{s}|^3}, \tag{B2}$$

where $r_v$ is an effective vortex tube radius, $l_\pm$ are the lengths of the line segments connected to $\boldsymbol{s}$ after discretization, and $\boldsymbol{s}'$ and $\boldsymbol{s}''$ are unit tangent and normal vectors at point $\boldsymbol{s}$, respectively. The first term on the right-hand side represents the LIA and typically gives the major contribution to $\boldsymbol{u}_s$. The vortex filament moves according to the total induced velocity $\mathrm{d}\boldsymbol{s}/\mathrm{d}t = \boldsymbol{u}_s(\boldsymbol{s}, t)$. Note that the vorticity distribution is assumed to be uniform within the tube radius, which is different from the Gaussian distribution in (3.4).

The VFM simulation is performed using the code QVORT developed by Hänninen & Baggaley (2014), where the finite difference scheme is employed for the spatial

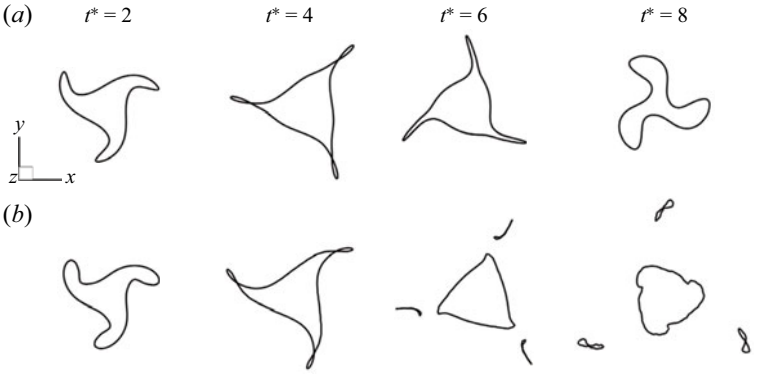


Figure 32. Evolution of the vortex core line calculated using the VFM for vortex $\mathcal{T}_{1,3}$ with $\lambda = 0.7$ and (*a*) $r_v = 0.025$ and (*b*) 0.05.

discretization, and the vortex filament is discretized by 1200 points. The third-order Adams–Bashforth method is used for time advance. Note that the VFM cannot handle vortex reconnection directly, so a 'cut and paste' algorithm is used to model the reconnection when the two vortices become too close to each other (Takaki & Hussain 1988; Baggaley 2012).

Figure 32(*a*,*b*) compares the evolutions of the vortex core line for vortex $\mathcal{T}_{1,3}$ with $r_v = 0.025$ and 0.05, where $r_v$ is set in the VFM simulation and $\lambda$ is chosen to be 0.7 for both cases. For $r_v = 0.05$, the tips of the petals are pinched off via reconnection, which is quite similar to that observed in figure 5(*d*) in DNS. In contrast, the vortex for $r_v = 0.025$ develops three petal-like branches under self-induction and then relaxes to a state close to the original shape. This difference suggests that the tube thickness can alter the stability of coiled vortex loops. The coiled loop tends to be more stable as the tube thickness decreases, i.e. $\lambda_c$ increases with decreasing $r_v$ or $\sigma$.

Note that as discussed in previous studies (Brenner, Hormoz & Pumir 2016; Yao & Hussain 2020*b*), the VFM has several limitations for studying vortex reconnection in viscous flows, especially for the characterization of the deformation of initially circular vortex cores and the treatment of vortex reconnection with bridging and threading processes. Therefore, an extensive study on the effect of the vortex tube thickness should be conducted using the DNS.

## Appendix C. Effects of the Reynolds number

Since the vortex tube thickness generally grows in viscous decaying flows, the Reynolds number can influence the torus aspect ratio. We further explore the effects of $Re$ on the critical torus aspect ratio $\lambda_c$ of vortex $\mathcal{T}_{1,q}$ by conducting a series of DNS cases with $Re = 4000$, $\sigma_0 = 1/(16\sqrt{2\pi})$ and various $\lambda$ on $N^3 = 1024^3$ grid points.

For a coiled vortex loop, the flow evolution can have a major difference from the quasi-periodic motion to reconnection within a small range of $\lambda$, but the precise value of $\lambda_c$ is hard to predict. Figure 33(*a*) shows the complex vortex dynamics for vortex $\mathcal{T}_{1,3}$ with $Re = 2000$ and $\lambda = 0.56$ – slightly less than $\lambda_c = 0.565$; $\lambda_c$ is determined by several numerical experiments. The outer edges of the vortex tube come into contact and then separate, but, in the mean time, generates a number of threads with strong interactions. This process is similar to the transition-like one caused by the incomplete reconnection for $\mathcal{T}_{2,q}$ at moderate $\lambda$ (see figure 26).

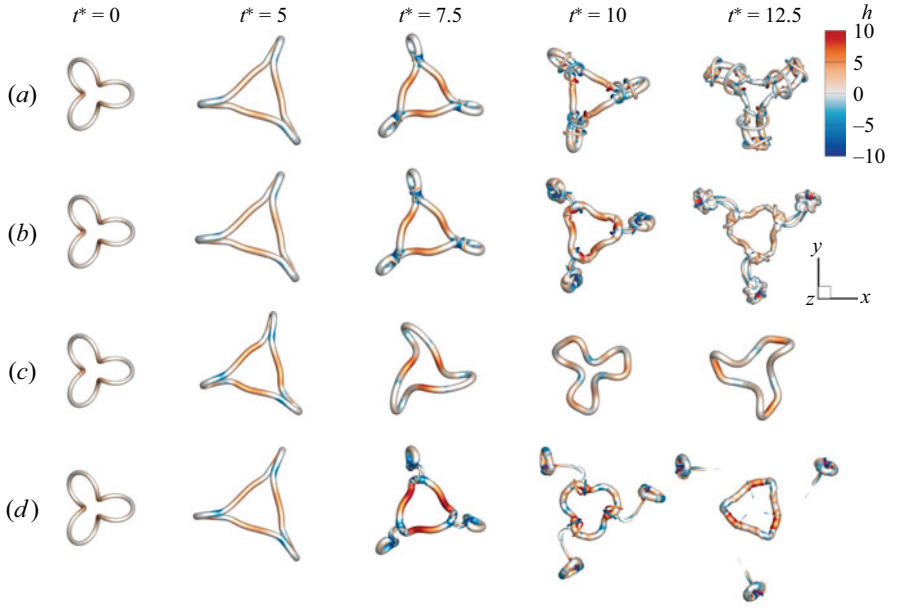


Figure 33. Evolution of the isosurface of $|\boldsymbol{\omega}| = 0.04\omega_0$ for vortex $\mathcal{T}_{1,3}$ with different $\lambda$ and $Re$: (*a*) $\lambda = 0.56$ and $Re = 2000$, (*b*) $\lambda = 0.565$ and $Re = 2000$, (*c*) $\lambda = 0.565$ and $Re = 4000$, (*d*) $\lambda = 0.605$ and $Re = 4000$. Surfaces are colour-coded by the helicity density.

Figure 33(*b*,*c*) compares evolutions of $\mathcal{T}_{1,3}$ with $\lambda = 0.565$ at $Re = 2000$ and 4000. The vortex loop undergoes the bridging reconnection at $Re = 2000$ around $\lambda_c$ with highly distorted vortical structures and multiple threads, while the reconnection does not occur at $Re = 4000$. Figure 33(*d*) suggests $\lambda_c = 0.605$ at $Re = 4000$. Since the growth of the tube thickness is suppressed at higher $Re$, $\lambda_c$ increases with $Re$, consistent with the conclusion with the VFM (see figure 32).

## Appendix D. On the conservation of the writhing number

### D.1. *Conservation of $W_r$ for isolated vortex tubes*

In general, the self-induced motion of vortex filaments can be approximated by the LIA, in which the deformation velocity is proportional to the local curvature of the vortex filament. Aldinger, Klapper & Tabor (1995) proved the conservation of $W_r$ for the curve evolution under the LIA. Note that the derivation based on the LIA does not consider the internal vorticity distribution in a vortex tube with a finite thickness.

Starting from the explicit expression of the initial vorticity field, we derive the rate of change of $H$ in a viscous flow to demonstrate the conservation of $W_r$ for a vortex tube with $T_w = 0$ and a finite thickness. The initial vortex tube is constructed from a given continuous and differentiable closed curve $\mathcal{C} : \boldsymbol{c}(s)$. The Frenet–Serret formulas on $\mathcal{C}$ are

$$\left.\begin{aligned} \frac{\mathrm{d}\boldsymbol{T}}{\mathrm{d}s} &= \kappa\boldsymbol{N}, \\ \frac{\mathrm{d}\boldsymbol{N}}{\mathrm{d}s} &= -\kappa\boldsymbol{T} + \tau\boldsymbol{B}, \\ \frac{\mathrm{d}\boldsymbol{B}}{\mathrm{d}s} &= -\tau\boldsymbol{N}, \end{aligned}\right\} \tag{D1}$$

where $\boldsymbol{T}, \boldsymbol{N}$ and $\boldsymbol{B} \equiv \boldsymbol{T} \times \boldsymbol{N}$ denote the unit tangent, normal and binormal vectors, respectively. The initial vorticity field with vanishing twist is constructed by (Xiong & Yang 2019*a*)

$$\boldsymbol{\omega}(s, \rho, \theta) = \Gamma f(\rho)\boldsymbol{T}(s). \tag{D2}$$

Its helicity $H = \Gamma^2 W_r$ is only proportional to the writhing number.

Curve $\mathcal{C}$ is considered as the central axis of the vortex tube by introducing the local polar coordinate system (Chui & Moffatt 1995), so Cartesian coordinates $\boldsymbol{x}$ can be expressed as

$$\boldsymbol{x} = \boldsymbol{c}(s) + \rho\cos\theta\boldsymbol{N} + \rho\sin\theta\boldsymbol{B}. \tag{D3}$$

From (D1) and (D3), we derive the Jacobian matrix

$$[(1 - \kappa\rho\cos\theta)\boldsymbol{T} - \tau\rho\sin\theta\boldsymbol{N} + \tau\rho\cos\theta\boldsymbol{B}; \cos\theta\boldsymbol{N} + \sin\theta\boldsymbol{B}; -\rho\sin\theta\boldsymbol{N} + \rho\cos\theta\boldsymbol{B}] \tag{D4}$$

for the transformation between coordinate systems $(s, \rho, \theta)$ and $(x, y, z)$.

The change rate of the total helicity in infinite space or in a periodic box is related to the volume integral of the super-helicity density in (A1). Substituting (D2) into the super-helicity term yields

$$\begin{aligned}\boldsymbol{\omega}\cdot(\nabla\times\boldsymbol{\omega}) &= \Gamma f(\rho)\boldsymbol{T}(s)\cdot[\nabla\times\Gamma f(\rho)\boldsymbol{T}(s)]\\ &= \Gamma^2 f(\rho)\boldsymbol{T}(s)\cdot\left[f(\rho)\nabla s\times\frac{\mathrm{d}\boldsymbol{T}(s)}{\mathrm{d}s} + \frac{\mathrm{d}f(\rho)}{\mathrm{d}\rho}\nabla\rho\times\boldsymbol{T}(s)\right].\end{aligned} \tag{D5}$$

Applying the inverse function theorem to (D4), we have

$$\nabla s = \frac{\boldsymbol{T}}{1 - \kappa\rho\cos\theta}, \quad \nabla\rho = \cos\theta\boldsymbol{N} + \sin\theta\boldsymbol{B}, \quad \nabla\theta = -\frac{\sin\theta}{\rho}\boldsymbol{N} + \frac{\cos\theta}{\rho}\boldsymbol{B}. \tag{D6$a$–$c$}$$

Substituting (D6) into (D5) yields

$$\boldsymbol{\omega}\cdot(\nabla\times\boldsymbol{\omega}) = \Gamma^2 f(\rho)\boldsymbol{T}\cdot\left[\frac{\kappa f(\rho)\boldsymbol{B}}{1 - \kappa\rho\cos\theta} + \frac{\mathrm{d}f(\rho)}{\mathrm{d}\rho}(\sin\theta\boldsymbol{N} - \cos\theta\boldsymbol{B})\right] = 0, \tag{D7}$$

and then we have $\mathrm{d}H/\mathrm{d}t = 0$ from (A1).

This result shows an ideal conservation of $H = \Gamma^2 W_r$ for a vortex tube with $T_w = 0$ in a viscous flow, so $W_r$ is almost conserved for Lamb–Oseen type vortices with negligible variations of $\Gamma$ during the time period of interest. On the other hand, when the vortex tube is reconnected or self-intersected, the vorticity distribution of the self-intersecting part does not satisfy (D2), so the total helicity has significant variations during vortex reconnection or merging.

### D.2. *Variation of $W_r$ during incomplete antiparallel reconnection*

The type of a curve intersection is specified in the directed projection graph in figure 34(*a*). If the minimum rotation angle from the arrow at the top to the one at the bottom is counterclockwise, the intersection has the index $+1$; if the angle is clockwise, the intersection index is $-1$. In addition to the integral definition (2.3), $W_r$ of a flat space curve close to a plane is approximated by the sum of the intersection indices in the curve projection on the plane (Fuller 1971; Scheeler *et al.* 2014).

Figure 34(*a*,*b*) sketches the changes of $W_r$ after the flat space curves with the initial $W_r \approx 1$ are reconnected at the antiparallel and the intersection points, respectively. By counting the interaction indices, it is straightforward to find that $W_r \approx 1$ maintains in

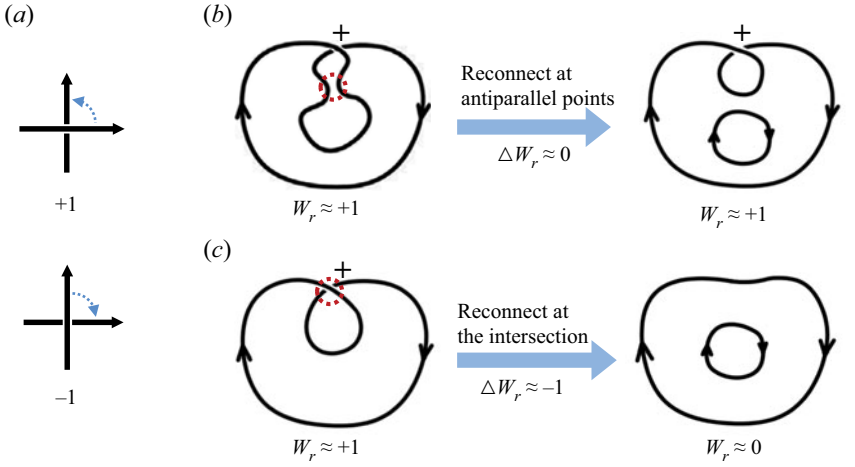


Figure 34. (*a*) The definition of positive and negative types of the curve intersection in the directed projection graph. Comparison of the writhe number variations $\Delta W_r$ during the reconnection of a flat space curve with initial $W_r \approx 1$ at (*b*) the antiparallel point and (*c*) the intersection point.

the antiparallel reconnection, whereas $W_r$ changes from 1 to 0 in the non-antiparallel reconnection. Laing, Ricca & Sumners (2015) also proved that $W_r$ is conserved during the antiparallel reconnection of the closed polyline.

On the other hand, for vortex tubes with finite thickness in viscous flows, the incipient antiparallel reconnection occurs from the periphery of vortex tubes where the approaching vortex lines are not perfectly antiparallel. As illustrated in figure 34, this imperfect antiparallel reconnection can cause the loss of $W_r$, so the writhe helicity is generally not conserved during the viscous reconnection.

## Appendix E. Decay of $\tilde{T}_w$ for twisted vortex tubes

We develop a model for the decay rate of $T_w$ of a uniformly twisted vortex tube constructed by the initial vorticity field (3.3) with constant $\eta$. In terms of the Frenet–Serret frame in (D1), (3.3) is re-expressed as

$$\boldsymbol{\omega}(s,\rho,\theta) = \Gamma f(\rho)\left[\boldsymbol{T}(s) - \frac{\eta\rho\sin\theta}{1-\kappa(s)\rho\cos\theta}\boldsymbol{N}(s) + \frac{\eta\rho\cos\theta}{1-\kappa(s)\rho\cos\theta}\boldsymbol{B}(s)\right]. \tag{E1}$$

We approximate the curved vortex tube or vortex loop by a straight tube, and then (E1) becomes

$$\boldsymbol{\omega}(s,\rho,\theta) = \Gamma f(\rho)\left[\boldsymbol{T} - \eta\rho\sin\theta\boldsymbol{N} + \eta\rho\cos\theta\boldsymbol{B}\right]. \tag{E2}$$

Taking the curl of the vorticity field in (E2), we have

$$\nabla\times\boldsymbol{\omega} = \Gamma\frac{\mathrm{d}f}{\mathrm{d}\rho}\nabla\rho\times\boldsymbol{T} - \eta\Gamma\left[\sin\theta\left(f+\rho\frac{\mathrm{d}f}{\mathrm{d}\rho}\right)\nabla\rho + \rho f\cos\theta\nabla\theta\right]\times\boldsymbol{N}$$
$$+\eta\Gamma\left[\cos\theta\left(f+\rho\frac{\mathrm{d}f}{\mathrm{d}\rho}\right)\nabla\rho - \rho f\sin\theta\nabla\theta\right]\times\boldsymbol{B}. \tag{E3}$$

Substituting (D6) into (E3) yields

$$\nabla\times\boldsymbol{\omega} = \Gamma\frac{\mathrm{d}f}{\mathrm{d}\rho}(\sin\theta\boldsymbol{N} - \cos\theta\boldsymbol{B}) + \eta\Gamma\left(2f+\rho\frac{\mathrm{d}f}{\mathrm{d}\rho}\right)\boldsymbol{T}. \tag{E4}$$

Thus, the super-helicity is

$$\boldsymbol{\omega}\cdot(\boldsymbol{\nabla}\times\boldsymbol{\omega}) = 2\eta\Gamma^2 f^2(\rho). \tag{E5}$$

By substituting (E5), (3.4) and (3.5) into (A1), the helicity change rate is

$$\frac{\mathrm{d}H}{\mathrm{d}t} = \frac{-\nu\eta\Gamma^2}{\pi^2\sigma^4}\iiint \exp\left(\frac{-\rho^2}{\sigma^2}\right)\rho\,\mathrm{d}\rho\,\mathrm{d}\theta\,\mathrm{d}s = \frac{-2\nu\Gamma^2 T_w}{\sigma^2}. \tag{E6}$$

Here, the vortex tube thickness grows as $\sigma = \sqrt{\sigma_0^2 + 2\nu(t-t_0)}$ in the viscous flow, where $\sigma_0$ denotes the initial vortex tube thickness and $t_0$ the initial time, and the helicity $H = \Gamma^2 T_w$ only contains the twist component. Assuming the circulation is constant in (E6), the decay rate of the twisting number is

$$\frac{\mathrm{d}T_w}{\mathrm{d}t} = \frac{-2\nu T_w}{\sigma_0^2 + 2\nu(t-t_0)}. \tag{E7}$$

Compared with $T_w$, the generalized twist formed in the viscous evolution, such as vortex merging, is not uniformly distributed along the vortex axis (see the non-uniform distribution of $h$ at $t^* = 0.5$ and 2.5 in figure 20). This modification is captured by a constant coefficient $k_g$ in the modelling of the decay rate of $\tilde{T}_w$ as

$$\frac{\mathrm{d}\tilde{T}_w}{\mathrm{d}t} = \frac{-2\nu k_g \tilde{T}_w}{\sigma_0^2 + 2\nu(t-t_0)}. \tag{E8}$$

Thus, we estimate the generalized twist

$$\tilde{T}_w(t) = \tilde{T}_w(t_0)\exp\left(\int_{t_0}^{t}\frac{-2\nu k_g}{\sigma_0^2 + 2\nu(t-t_0)}\,\mathrm{d}t\right) \tag{E9}$$

for a twisted vortex tube.

For the vortex merging case in § 5.1, we apply the helicity topological relationship $H = \Gamma^2\tilde{T}_w = 4\Gamma_0^2\tilde{T}_w$ and the dimensionless time $t^* = t/(R_t^2/\Gamma_0)$ to (E9), and then obtain a helicity model after the vortex merging event as

$$H(t^*) = H(t_m^*)\exp\left(\int_{t_m^*}^{t^*}\frac{-2\nu k_g R_t^2}{\sigma(t_m^*)^2\Gamma_0 + 2\nu R_t^2(t^* - t_m^*)}\,\mathrm{d}t^*\right), \quad t^* > t_m^*, \tag{E10}$$

where $k_g = 0.75$ is fitted from the DNS result of $H(t^* > t_m^*)$.

## References


Adams, C.C. 1994 *The Knot Book*. American Mathematical Society.

Aldinger, J., Klapper, I. & Tabor, M. 1995 Formulae for the calculation and estimation of writhe. *J. Knot Theory Ramif.* **4**, 343–372.

Aref, H. & Zawadzki, I. 1991 Linking of vortex rings. *Nature* **354**, 50–53.

Baggaley, A.W. 2012 The sensitivity of the vortex filament method to different reconnection models. *J. Low Temp. Phys.* **168**, 18–30.

Barenghi, C.F. 2007 Knots and unknots in superfluid turbulence. *Milan J. Maths* **75**, 177–196.

Barenghi, C.F., Hänninen, R. & Tsubota, M. 2006 Anomalous translational velocity of vortex ring with finite-amplitude Kelvin waves. *Phys. Rev.* E **74**, 046303.

Berger, M.A. & Field, G.B. 1984 The topological properties of magnetic helicity. *J. Fluid Mech.* **147**, 133–148.

BETCHOV, R. 1965 On the curvature and torsion of an isolated vortex filament. *J. Fluid Mech.* **22**, 471–479.
BRENNER, M.P., HORMOZ, S. & PUMIR, A. 2016 Potential singularity mechanism for the Euler equations. *Phys. Rev. Fluids* **1**, 084503.
BRISSAUD, A., FRISCH, U., LÉORAT, J., LESIEUR, M. & MAZURE, A. 1973 Helicity cascades in fully developed isotropic turbulence. *Phys. Fluids* **16**, 1366–1367.
CHUI, A.Y.K. & MOFFATT, H.K. 1995 The energy and helicity of knotted magnetic flux tubes. *Proc. R. Soc. Lond.* A **451**, 609–629.
CIRTAIN, J.W., *et al.* 2013 Energy release in the solar corona from spatially resolved magnetic braids. *Nature* **493**, 501–503.
DENNIS, M.R., KING, R.P., JACK, B., O'HOLLERAN, K. & PADGETT, M.J. 2010 Isolated optical vortex knots. *Nat. Phys.* **6**, 118–121.
FUENTES, O.V. 2010 Chaotic streamlines in the flow of knotted and unknotted vortices. *Theor. Comput. Fluid Dyn.* **24**, 189–193.
FULLER, F.B. 1971 The writhing number of a space curve. *Proc. Natl Acad. Sci. USA* **68**, 815–819.
GRIFFITHS, R.W. & HOPFINGER, E.J. 1987 Coalescing of geostrophic vortices. *J. Fluid Mech.* **178**, 73–97.
HAMA, F.R. 1962 Progressive deformation of a curved vortex filament by its own induction. *Phys. Fluids* **5**, 1156–1162.
HÄNNINEN, R. & BAGGALEY, A.W. 2014 Vortex filament method as a tool for computational visualization of quantum turbulence. *Proc. Natl Acad. Sci. USA* **111**, 4667–4674.
HAO, J. & YANG, Y. 2021 Magnetic knot cascade via the stepwise reconnection of helical flux tubes. *J. Fluid Mech.* **912**, A48.
HASIMOTO, H. 1972 A soliton on a vortex filament. *J. Fluid Mech.* **51**, 477–485.
HIDE, R. 1989 Superhelicity, helicity and potential vorticity. *Geophys. Astrophys. Fluid Dyn.* **48**, 69–79.
IRVINE, W.T.M. & BOUWMEESTER, D. 2008 Linked and knotted beams of light. *Nat. Phys.* **4**, 716–720.
KEENER, J.P. 1990 Knotted vortex filaments in an ideal fluid. *J. Fluid Mech.* **211**, 629–651.
KERR, R.M. 2018*a* Enstrophy and circulation scaling for Navier–Stokes reconnection. *J. Fluid Mech.* **839**, R2.
KERR, R.M. 2018*b* Topology of interacting coiled vortex rings. *J. Fluid Mech.* **854**, R2.
KERR, R.M. 2018*c* Trefoil knot timescales for reconnection and helicity. *Fluid Dyn. Res.* **50**, 011422.
KIDA, S. 1981 A vortex filament moving without change of form. *J. Fluid Mech.* **112**, 397–409.
KIDA, S. & TAKAOKA, M. 1987 Bridging in vortex reconnection. *Phys. Fluids* **30**, 2911–2914.
KIDA, S. & TAKAOKA, M. 1988 Reconnection of vortex tubes. *Fluid Dyn. Res.* **3**, 257–261.
KIDA, S. & TAKAOKA, M. 1991 Breakdown of frozen motion of vorticity field and vorticity reconnection. *J. Phys. Soc. Japan* **60**, 2184–2196.
KIDA, S. & TAKAOKA, M. 1994 Vortex reconnection. *Annu. Rev. Fluid Mech.* **26**, 169–177.
KIDA, S., TAKAOKA, M. & HUSSAIN, F. 1991 Collision of two vortex rings. *J. Fluid Mech.* **230**, 583–646.
KIMURA, Y. & MOFFATT, H.K. 2017 Scaling properties towards vortex reconnection under Biot–Savart evolution. *Fluid Dyn. Res.* **50**, 011409.
KIVOTIDES, D. & LEONARD, A. 2021 Helicity spectra and topological dynamics of vortex links at high Reynolds numbers. *J. Fluid Mech.* **911**, A25.
KLECKNER, D. & IRVINE, W.T.M. 2013 Creation and dynamics of knotted vortices. *Nat. Phys.* **9**, 253–258.
KLECKNER, D., KAUFFMAN, L.H. & IRVINE, W.T.M. 2016 How superfluid vortex knots untie. *Nat. Phys.* **12**, 650–655.
KLOTZ, A.R., SOH, B.W. & DOYLE, P.S. 2018 Motion of knots in DNA stretched by elongational fields. *Phys. Rev. Lett.* **120**, 188003.
LAING, C.E., RICCA, R.L. & SUMNERS, D.W. 2015 Conservation of writhe helicity under anti-parallel reconnection. *Sci. Rep.* **5**, 1–6.
LE DIZES, S. & VERGA, A. 2002 Viscous interactions of two co-rotating vortices before merging. *J. Fluid Mech.* **467**, 389–410.
LEVY, Y., DEGANI, D. & SEGINER, A. 1990 Graphical visualization of vortical flows by means of helicity. *AIAA J.* **28**, 1347–1352.
LIU, X., RICCA, R.L. & LI, X.-F. 2020 Minimal unlinking pathways as geodesics in knot polynomial space. *Commun. Phys.* **3**, 136.
MARTINEZ, A., RAVNIK, M., LUCERO, B., VISVANATHAN, R., ŽUMER, S. & SMALYUKH, I.I. 2014 Mutually tangled colloidal knots and induced defect loops in nematic fields. *Nat. Mater.* **13**, 258–263.
MAXWORTHY, T. 1977 Some experimental studies of vortex rings. *J. Fluid Mech.* **81**, 465–495.
MELANDER, M.V. & HUSSAIN, F. 1988 Cut-and-connect of two antiparallel vortex tubes. In *Studying Turbulence Using Numerical Simulation Databases*, vol. 2, pp. 257–286. Center for Turbulence Research.
MELANDER, M.V., ZABUSKY, N.J. & MCWILLIAMS, J.C. 1988 Symmetric vortex merger in two dimensions: causes and conditions. *J. Fluid Mech.* **195**, 303–340.

MILNOR, J. & WEAVER, D.W. 1997 *Topology from the Differentiable Viewpoint*. Princeton University Press.
MOFFATT, H.K. 1969 The degree of knottedness of tangled vortex lines. *J. Fluid Mech.* **35**, 117–129.
MOFFATT, H.K. 2021 Some topological aspects of fluid dynamics. *J. Fluid Mech.* **914**, 43–48.
MOFFATT, H.K., KIDA, S. & OHKITANI, K. 1994 Stretched vortices–the sinews of turbulence; large-Reynolds-number asymptotics. *J. Fluid Mech.* **259**, 241–264.
MOFFATT, H.K. & RICCA, R.L. 1992 Helicity and the Călugăreanu invariant. *Proc. R. Soc. Lond.* A **439**, 411–429.
MOFFATT, H.K. & TSINOBER, A. 1992 Helicity in laminar and turbulent flow. *Annu. Rev. Fluid Mech.* **24**, 281–312.
MOREAU, J.J. 1961 Constantes d'un îlot tourbillonnaire en fluide parfait barotrope. *C. R. Acad. Sci. Paris* **252**, 2810–2812.
OBERTI, C. & RICCA, R.L. 2016 On torus knots and unknots. *J. Knot Theory Ramif.* **25**, 1650036.
OBERTI, C. & RICCA, R.L. 2019 Influence of winding number on vortex knots dynamics. *Sci. Rep.* **9**, 17284.
POPE, S.B. 2000 *Turbulent Flows*. Cambridge University Press.
PROMENT, D., ONORATO, M. & BARENGHI, C.F. 2012 Vortex knots in a Bose–Einstein condensate. *Phys. Rev.* E **85**, 036306.
RICCA, R.L. & BERGER, M.A. 1996 Topological ideas and fluid mechanics. *Phys. Today* **49**, 28–34.
RICCA, R.L., SAMUELS, D.C. & BARENGHI, C.F. 1999 Evolution of vortex knots. *J. Fluid Mech.* **391**, 29–44.
SCHEELER, M.W., KLECKNER, D., PROMENT, D., KINDLMANN, G.L. & IRVINE, W.T.M. 2014 Helicity conservation by flow across scales in reconnecting vortex links and knots. *Proc. Natl Acad. Sci. USA* **111**, 15350–15355.
SCHEELER, M.W., VAN REES, W.M., KEDIA, H., KLECKNER, D. & IRVINE, W.T.M. 2017 Complete measurement of helicity and its dynamics in vortex tubes. *Science* **357**, 487–491.
SCHWARZ, K.W. 1985 Three-dimensional vortex dynamics in superfluid He 4: Line-line and line-boundary interactions. *Phys. Rev.* B **31**, 5782.
TAKAKI, R. & HUSSAIN, F. 1988 Singular interaction of vortex filaments. *Fluid Dyn. Res.* **3**, 251.
THOMSON, W. 1878 Vortex statics. *Proc. R. Soc. Edin.* **9**, 59–73.
TKALEC, U., RAVNIK, M., ČOPAR, S., ŽUMER, S. & MUŠEVIČ, I. 2011 Reconfigurable knots and links in chiral nematic colloids. *Science* **333**, 62–65.
WASSERMAN, S.A. & COZZARELLI, N.R. 1986 Biochemical topology: applications to DNA recombination and replication. *Science* **232**, 951–960.
XIONG, S. & YANG, Y. 2019*a* Construction of knotted vortex tubes with the writhe-dependent helicity. *Phys. Fluids* **31**, 047101.
XIONG, S. & YANG, Y. 2019*b* Identifying the tangle of vortex tubes in homogeneous isotropic turbulence. *J. Fluid Mech.* **874**, 952–978.
XIONG, S. & YANG, Y. 2020 Effects of twist on the evolution of knotted magnetic flux tubes. *J. Fluid Mech.* **895**, A28.
YANG, Y., PULLIN, D.I. & BERMEJO-MORENO, I. 2010 Multi-scale geometric analysis of Lagrangian structures in isotropic turbulence. *J. Fluid Mech.* **654**, 233–270.
YAO, J. & HUSSAIN, F. 2020*a* A physical model of turbulence cascade via vortex reconnection sequence and avalanche. *J. Fluid Mech.* **883**, A53.
YAO, J. & HUSSAIN, F. 2020*b* On singularity formation via viscous vortex reconnection. *J. Fluid Mech.* **888**, R2.
YAO, J. & HUSSAIN, F. 2022 Vortex reconnection and turbulence cascade. *Annu. Rev. Fluid Mech.* **54**, 317–347.
YAO, J., YANG, Y. & HUSSAIN, F. 2021 Dynamics of a trefoil knotted vortex. *J. Fluid Mech.* **923**, A19.
ZHAO, X. & SCALO, C. 2021 Helicity dynamics in reconnection events of topologically complex vortex flows. *J. Fluid Mech.* **920**, A30.
ZHAO, X., YU, Z., CHAPELIER, J.-B. & SCALO, C. 2021 Direct numerical and large-eddy simulation of trefoil knotted vortices. *J. Fluid Mech.* **910**, A31.
ZHENG, T., YOU, J. & YANG, Y. 2017 Principal curvatures and area ratio of propagating surfaces in isotropic turbulence. *Phys. Rev. Fluids* **2**, 103201.
ZUCCHER, S. & RICCA, R.L. 2017 Relaxation of twist helicity in the cascade process of linked quantum vortices. *Phys. Rev.* E **95**, 053109.